Actively forming Kuroko-type volcanic-hosted massive sulfide (VHMS) mineralization at Iheya North, Okinawa Trough, Japan

Actively forming Kuroko-type volcanic-hosted massive sulfide (VHMS) mineralization at Iheya North, Okinawa Trough, Japan

Christopher J. Yeats[1,2], Steven P. Hollis[1,3*], Angela Halfpenny[1,4], Juan-Carlos Corona[5], Crystal LaFlamme[6], Gordon Southam[7], Marco Fiorentini[6], Richard J. Herrington[8] & John Spratt[8]

[1]CSIRO, Mineral Resources, 26 Dick Perry Avenue, Kensington, Perth, Western Australia, 6151, Australia
[2]Geological Survey of New South Wales, NSW Department of Industry, 516 High St, Maitland, NSW, 2320, Australia
[3]iCRAG (Irish Centre for Research in Applied Geosciences) and School of Earth Sciences, University College Dublin, Belfield, Dublin 4, Ireland
[4]Microscopy & Microanalysis Facility, John de Laeter Center , Curtin University, Perth, Western Australia, 6102 , Australia
[5]Department of Geological Sciences and Environmental Studies, Binghamton University, Binghamton, NY, 13902, USA
[6]Centre for Exploration Targeting, School of Earth and Environment, University of Western Australia (M006), ARC Centre of Excellence for Core to Crust Fluid Systems, 35 Stirling Highway, Perth, Western Australia, 6009, Australia
[7]School of Earth Sciences, The University of Queensland, St Lucia, Queensland, 4072, Australia
[8]Department of Earth Sciences, Natural History Museum, London, SW7 5BD, UK

For: *Ore Geology Reviews (IF 3.558)*

Keywords: volcanogenic massive sulfide, VMS, hydrothermal, IODP, black smoker, EBSD

***Corresponding author:** steve.hollis@icrag-centre.org

ABSTRACT

Modern seafloor hydrothermal systems provide important insights into the formation and discovery of ancient volcanic-hosted massive sulfide (VHMS) deposits. In 2010, Integrated Ocean Drilling Program (IODP) Expedition 331 drilled five sites in the Iheya North hydrothermal field in the middle Okinawa Trough, back-arc basin, Japan. Hydrothermal alteration and sulfide mineralization is hosted in a geologically complex, mixed sequence of coarse, pumiceous, volcaniclastic and fine hemipelagic sediments, overlying a dacitic to rhyolitic volcanic substrate. At site C0016, located adjacent to the foot of the actively venting North Big Chimney massive sulfide mound, massive sphalerite-(pyrite-chalcopyrite±galena)-rich sulfides were intersected (to 30.2% Zn, 12.3% Pb, 2.68% Cu, 33.1 ppm Ag and 0.07 ppm Au) that strongly resemble the black ore of the Miocene-age Kuroko deposits of Japan. Sulfide mineralization shows clear evidence of formation through a combination of surface detrital and subsurface chemical processes, with at least some sphalerite precipitating into void space in the rock. Volcanic rocks beneath massive sulfides exhibit quartz-muscovite/illite and quartz-Mg-chlorite alteration reminiscent of VHMS proximal footwall alteration associated with Kuroko-type deposits, characterised by increasing MgO, Fe/Zn and Cu/Zn with depth. Recovered felsic footwall rocks are of FII to FIII affinity with well-developed negative Eu anomalies, consistent with VHMS-hosting felsic rocks in Phanerozoic ensialic arc/back-arc settings worldwide.

Site C0013, ~100 m east of North Big Chimney, represents a likely location of recent high temperature discharge, preserved as surficial coarse-grained sulfidic sediments (43.2% Zn, 4.4% Pb, 5.4% Cu, 42 ppm Ag and 0.02 ppm Au) containing high concentrations of As, Cd, Mo, Sb, and W. Near surface hydrothermal alteration is dominated by kaolinite and muscovite with locally abundant native sulfur, indicative of acidic hydrothermal fluids. Alteration grades to Mg-chlorite dominated assemblages at depths of >5 mbsf (metres below sea floor). Late coarse-grained anhydrite veining overprints earlier alteration and is interpreted to have precipitated from down welling seawater as hydrothermal activity waned. At site C0014, ~350 m farther east, hydrothermal assemblages are characterized by illite/montmorillonite, with Mg-chlorite present at depths below ~30 mbsf. Recovered lithologies from distal, recharge site C0017 are unaltered, with low MgO, Fe_2O_3 and base metal concentrations.

Mineralization and alteration assemblages are consistent with the Iheya North system representing a modern analogue for Kuroko-type VHMS mineralization. Fluid flow is focussed laterally along pumiceous volcaniclastic strata (compartmentalized between impermeable

hemipelagic sediments), and vertically along faults. The abundance of Fe-poor sphalerite and Mg-rich chlorite (clinochlore/penninite) is consistent with the lower Fe budget, temperature and higher oxidation state of felsic volcanic-hosted hydrothermal systems worldwide compared to Mid Ocean Ridge black smoker systems.

1. INTRODUCTION

Over the past 25 years our understanding of seafloor hydrothermal fields has been revolutionized by the research activity of the Deep Sea Drilling Project (1968-1983), Ocean Drilling Program (ODP; 1985-2003) and Integrated Ocean Drilling Program (IODP; 2004-2013). In particular, the research findings of expeditions to the Trans-Atlantic Geotraverse [TAG], Manus Basin and Juan de Fuca Ridge have provided important insights into the nature of fluid rock interaction and fluid mixing in the development of seafloor hydrothermal systems in different tectonic settings (Barriga et al., 2000; Fouquet et al., 1997; Humphris et al., 1995, 1998; Lackschewitz et al., 2004; Mottl et al., 1994; Paulick and Bach, 2006; Roberts et al., 2003; Teagle et al., 1998; Webber et al., 2011). This work has been complemented by countless other scientific and industry-funded cruises to hydrothermal fields worldwide (Connelly et al., 2012; de Ronde et al., 2005; Glasby et al., 2008; Hannington et al., 2005 and references therein; Ishibashi et al., 2015; McConachy et al., 2005; Petersen et al., 2014; Yeats et al., 2014; Webber et al., 2015).

Volcanic-hosted massive sulfide (VHMS) deposits represent significant resources of base and precious metals in a number of Archean Cratons and Phanerozoic volcanic arcs/back-arc basins worldwide (Barrie et al., 1993; Galley et al., 1993; Herrington et al., 2005; Hollis et al., 2015; van Staal, 2007). VHMS mineralization occurs as syngenetic stratiform accumulations of metal sulfides that precipitated at or below the seafloor, often underlain by discordant zones of stringer and disseminated sulfides (Franklin et al., 2005). The size, metallogeny and grade of a deposit that forms within a volcanic succession is dependent on its tectonic setting, host lithologies and any magmatic input (Barrie and Hannington, 1999; de Ronde et al., 2003, 2005; Piercey, 2011). Therefore, analogues for specific types of VHMS deposits are represented by different modern hydrothermal systems (e.g. Glasby et al., 2008; Hannington et al., 1998; Ishibashi and Urabe, 1995; Lüders et al., 2001; Webber et al., 2015). Active systems provide important insights into the formation of ancient VHMS deposits, allowing fluids to be directly sampled and mineralization to be studied without the effects of subsequent deformation and metamorphism.

Hydrothermal vents were first discovered at the Iheya North Knoll in 1995 (**Fig. 1**), and this location has since become the most intensely investigated of all hydrothermal fields within the middle Okinawa Trough, Japan (Aoyama et al., 2014; Chiba et al., 1996; Glasby and Notsu, 2003; Ishibashi et al., 2015; Kawagucci et al., 2013; Masaki et al., 2011; Shao et al., 2015; Takai et al., 2011; Tsuji et al., 2012). During 2010, IODP Expedition 331 drilled five sites at Iheya North. Blocks of massive and semi-massive sphalerite-(pyrite-chalcopyrite±galena)-rich sulfides, that strongly resembled the 'black ore' of the Kuroko VHMS deposits of Japan, were recovered from immediately beneath the modern seafloor (Takai et al., 2011). Samples collected during IODP Expedition 331 provide a unique opportunity to understand hydrothermal fluid flow and mineralization processes associated with an actively forming Kuroko-style VHMS deposit in an ensialic back-arc setting. We present shipboard logging and X-ray diffraction data, along with new petrographic, whole rock geochemical, mineral-chemical and microstructural work on recovered lithologies.

2. REGIONAL GEOLOGY

The Okinawa Trough, Japan, extends for ~1200 km between the Ryukyu arc-trench system and the Eurasian continent, and is regarded as an incipient intra-continental back-arc basin (Lee et al., 1980; Letouzey and Kimura, 1986; Shinjo and Kato, 2000; **Fig. 1a**). It is still considered to be in an early rifting stage prior to seafloor spreading (Shinjo and Kato, 2000), with a minimal crustal thickness of ~8 km at its southernmost end (Klingelhoefer et al., 2009). Arc volcanism predominantly occurs in the northern part of the Ryukyu Arc and in the middle and southern parts of the Okinawa Trough (Shinjo et al., 2000). The transition from arc to back-arc volcanism in the middle Okinawa Trough has been termed the VAMP area (Sibuet et al., 1987), with present day activity in the middle and southern Okinawa Trough associated with *en echelon* intra-trough grabens (Glasby and Notsu, 2003; Shinjo and Kato, 2000). The VAMP area is coincident with the subduction of the WNW-ENE trending Daito Ridge (Sibuet et al., 1998; **Fig. 1a**). A rift-related bimodal basaltic-rhyolitic suite, accompanied by minor intermediate rocks, characterizes the middle Okinawa Trough (Ishizuka et al., 1990; Shinjo et al., 1999; Shinjo and Kato, 2000; Zeng et al., 2010). Thick (~1000 m) sequences of organic-rich terrigenous sediments sourced from the Yangtze and Yellow rivers overlie basement lithologies (Takai et al., 2011). Due to volcanism and rifting, the VAMP area is characterized by anomalously high heat flow (Yamano et al., 1986) and contains several hydrothermal fields (Glasby and Notsu, 2003; Ishibashi et al., 2015). From north to south these include the Minami-

Ensei Knoll, Iheya North Knoll (**Fig. 1b-c**), Yoron Hole, CLAM site of the Iheya Ridge, the JADE and Hakueri hydrothermal fields of the Izena Hole (also known as the Izena Cauldron) (Ishibashi et al., 2015).

3. HYDROTHERMAL ACTIVITY AT IHEYA NORTH

The Iheya North Knoll hydrothermal field is located at ~1000 mbsl (metres below sea level) in the middle Okinawa Trough (**Fig. 1b**). Approximately ten hydrothermal mounds aligned north to south are associated with active venting and sulfide/sulfate mineralization (Ishibashi et al., 2015; **Fig. 1c**). The main sulfide assemblages identified from chimney samples are dominated by sphalerite, wurtzite [(Zn,Fe)S], galena, pyrite, marcasite [FeS_2] and chalcopyrite (Ueno et al., 2003). Some samples also include arsenopyrite, tetrahedrite [$Cu_{12}(As,Sb)_4S_{13}$], tennantite [$Cu_3(As,Sb)_4$], freslebenite [$PbAgSbS_3$], native arsenic, realgar [AsS] and/or covellite [CuS] (Ueno et al., 2003). Gangue mineralogy is characterized by barite, gypsum, anhydrite, quartz, rhodochrosite [$MnCO_3$], and/or native sulfur (Chiba, 1997; Ueno et al., 2003).

Recent studies of hydrothermal fluid chemistry at Iheya North indicate the presence of high concentrations of CO_2, CH_4, NH_4^+, B, and I, and high alkalinity, consistent with some interaction between hydrothermal fluids and organic matter (Kawagucci et al., 2011), although this is less pronounced than at the JADE and CLAM sites. High concentrations of K, Rb, Cs and Li in interstitial water are consistent with interaction between hydrothermal fluids and felsic footwall lithologies (Takai et al., 2011). North Big Chimney (NBC) marks the centre of the hydrothermal field and is associated with the vigorous venting of clear fluid of 311 °C at 971 mbsl (Nakagawa et al., 2005; **Fig. 1c**). The chimney is 20 m high and 6 m in diameter (Takai et al., 2011). Chloride concentrations lower than seawater suggest phase separation at depth (Chiba et al., 1996).

During IODP Expedition 331, five sites were drilled at Iheya North (C0013 to C0017; **Figs. 1b-c, 2**). Hydrothermal alteration and sulfide mineralization is hosted in a geologically complex mixed sequence of coarse pumiceous, volcaniclastic, and fine, hemipelagic, sediments, overlying dacitic to rhyolitic volcanic substrate. Site descriptions (section 5) are based on shipboard data (detailed in Takai et al., 2011, 2012) and post-cruise research. Post-drilling changes in fluid flow and chemistry at sites C0014 and C0016 are detailed in Kawagucci et al. (2013).

4. METHODS

During IODP Expedition 331, approximately 325 powdered whole rock samples were analysed by X-ray diffraction (XRD) to characterize the main alteration minerals present across the Iheya North hydrothermal field. Samples of interest were also examined using polished thin sections and scanning-electron microscopy (SEM). Post-cruise research focussed primarily on the whole rock geochemical, mineral-chemical and microstructural characterization of recovered lithologies.

Shipboard SEM analysis was conducted using a GEOL 5770 SEM equipped with backscatter and energy dispersive spectroscopy detectors operating at an accelerating voltage of 15 kV. Samples for XRD were systematically analysed from every 1.5 m section of core obtained during hydraulic piston coring and extended shoe coring, and for every 0.75 m core section for Baker Hughes INTEQ (BHI) cores. Additional samples were analysed as deemed appropriate. Samples were freeze-dried prior to powdering in a ball mill. Powders were analysed on a PANalytical CubiX PRO (PW3800) diffractometer. Further detail is provided by Takai et al. (2011).

For post-cruise research, samples from site C0016 were imaged using both secondary electrons (SE) and backscattered electrons (BSE) in a Zeiss Ultraplus field emission gun (FEG) SEM at the CSIRO facilities, Kensington, Western Australia, operated at a chamber pressure of $2x10^{-6}$ mbar and an accelerating voltage of 20 kV.

Twenty-five specimens (samples IN01-IN25) representative from each of the five sites (C0013 to C0017) were submitted for whole-rock geochemical analysis to Bureau Veritas Geoanalytical Laboratory, Canning Vale, Western Australia, to characterize the geochemistry of the host sequence and the intensity of hydrothermal alteration. Samples were predominantly composed of variably hydrothermally altered and/or mineralized, felsic pumiceous volcaniclastic sediments and basement rocks, with one sample of hemipelagic clay (IN08; **Table 1**). Major element concentrations (plus S, Cu, Pb, Zn, Ba) were determined on fused glass beads (using a 12:22 flux ratio and 4% lithium nitrate) by X-ray Fluorescence (XRF). Trace elements were determined on the same fused discs by laser ablation inductively coupled plasma mass spectrometry (LA-ICP-MS). Gold, Pt and Pd were analysed by lead-collection fire assay with element concentrations quantified by ICP-MS. Carbon concentrations were measured by total combustion using a Carbon-Sulfur Analyser. Loss on ignition (LOI) was calculated using a robotic thermogravimetric system set to 110 and 1000 °C. Sulfate concentrations were determined by digestion with hydrochloric acid and evaporation to dryness twice before a final leach in hydrochloric acid. Results are presented in **Table 1**.

Accuracy (% RD) was monitored using mineralized (to 34.6% Zn, 13.2% Pb, 3.1% Cu) and unmineralized international standards. Precision (% RSD) was monitored by repeat analysis of samples from Iheya North. Accuracy and precision can be considered good to excellent after Jenner (1996) for all elements determined by XRF, except for Al_2O_3, MgO, MnO and P_2O_5 in some instances where concentrations were near detection (i.e. 0.01 wt.%). Accuracy for elements determined by LA-ICP-MS was good to excellent (<10% RD) except for As at low concentrations, and Cd. Precision was also poor (>10% RSD) for Cd and consequently these data should be treated with caution. Accuracy and precision for Au, Pt, Pd and C were good to excellent for all standards used after Jenner (1996).

Mineral compositions of chlorite and white mica from site C0016B were determined at the Natural History Museum, London, on a Cameca SX-50 Electron Microprobe (EMP) equipped with a wavelength dispersive system (WDS). Operating conditions were at 20 keV and 20 nA. Counting times ranged from 10 to 50 s for spot analysis. Chlorite mineral formulae were calculated using the worksheets of Tindle (2015).

For EBSD analysis, round samples (25 mm in diameter) were polished using colloidal silica for 5 hours on a Buehler Vibromat 1, and for 1 hour on the Leica Microsystems EM RES101 instrument (after Halfpenny, 2010; Halfpenny et al., 2013). Full crystallographic orientation data were obtained from automatically indexed Kikuchi diffraction patterns collected using a Bruker e-flash detector fitted to a Zeiss Ultraplus FEG SEM at the CSIRO facilities, Kensington. Coincident EDS data were collected using a Bruker XFlash 5030 detector. The SEM was operated using an accelerating voltage of 20 kV and a 120 µm aperture, which in high current mode produced a beam current of 12.1 nA. The EBSD data were collected using the Bruker Quantax Espirit 1.9 software, using a resolution of 200 x 150 pixels, a 12 ms exposure time and a step size between measurements of 1.7 µm. If the pattern quality was poor then the software was unable to find the correct crystallographic solution and the point was not indexed. Non-indexed points are common in areas of poor surface quality, on grain boundaries, cracks, void space and where the surface is contaminated. Unfortunately, not all of the sample was prepared well enough for EBSD analysis, due to the various hardnesses of the constituent phases, this has led to areas of non-indexing. The EBSD data were post-processed using Oxford Instruments Channel 5 software to remove mis-indexed points and interpolate non-indexed points (Prior et al., 2009; Halfpenny, 2010). The corrected data files were then used to generate the maps presented.

5. RESULTS

224 **5.1 Hydrothermal alteration and mineralization at Iheya North**

225 **Site C0016 (North Big Chimney)**

226 Site C0016 is located at North Big Chimney (**Fig. 1c**). Although hole C0016A at the
227 summit of NBC failed to recover core, a variety of lithologies were obtained from hole C0016B
228 drilled at its base (**Fig. 3f-j**). From 45 m of drilling at C0016B, only 2.1 m of core was recovered
229 (4.7% recovery). Between 0 and 9 mbsf, blocks of massive and semi-massive sphalerite-rich
230 sulfide were recovered (**Fig. 3f** –1 to 3), along with a 15cm section of silicified and mineralized
231 volcanic rock altered to illite/muscovite clay (confirmed by XRD; **Fig. 3g**). Recovered sections
232 of clastic-textured massive/semi-massive sulfide (**Fig. 3f** – blocks 1 to 3) are characterized by
233 rounded 1-5 mm fragments of clay-altered and hard siliceous volcanic rock, cemented by a
234 matrix of sphalerite (~60%), pyrite (~15%) and quartz, with lesser galena and chalcopyrite
235 (**Figs. 3f; 4a**). Silicification is variable, with the uppermost block containing coarser grained
236 (2-3 mm) sphalerite-pyrite-galena-(chalcopyrite) associated with late anhydrite veining (**Fig.**
237 **3f**). The second section of core obtained from 9-27 mbsf (31 cm total recovery) included two
238 pieces of hydrothermally altered, silicified and mineralized volcanic rock with clastic textures,
239 found either side of a 12 cm piece of coarsely crystalline white acicular anhydrite cut by thin
240 veins of sphalerite-pyrite (**Fig. 3h** - blocks 5-7). The third section of core (from 27-45 mbsf)
241 comprised almost 1m of quartz-chlorite altered volcanic rock exhibiting stockwork veining of
242 quartz-chlorite-pyrite and late anhydrite (**Fig. 3i-j –** blocks 8-9). XRD analysis identified the
243 chlorite as clinochlore (Mg-chlorite) – subsequently confirmed by electron microprobe
244 analysis. Two generations of veining have been recognized: (i) early sugary, 2-3 cm wide
245 quartz-chlorite-pyrite veins which form a dark network; and (ii) late vuggy pyrite-anhydrite
246 veins, from hairline to 1 cm in thickness.

247

248 **Site C0013 (a site of recent hydrothermal activity):**

249 Site C0013, located ~100 m east of NBC (Fig. 1c), is characterized by numerous areas
250 of patchy diffuse flow and chemosynthetic animal colonies, where the seafloor is covered by
251 pumiceous breccias and barite-anhydrite-carbonate crusts, with hemipelagic sediment in
252 depressions (Takai et al., 2012). Site C0013 occurs in a zone of relatively high heat flow,
253 estimated before drilling to be ~3 °C/m (Takai et al., 2012). Eight holes were sited to a
254 maximum depth of 54.3 mbsf (hole C0013E; Fig. 2a). Melting of plastic core liners severely
255 limited drilling to depth, with core liners starting to soften and deform at 12 mbsf and 82 °C.
256 Following capping and casing of the deepest hole, strong hydrothermal discharge was noted by
257 ROV from the casing pipe, with thermoseal temperature-sensitive strips indicating

258 temperatures >250 °C. Two days later blackish water was discharging directly from the hole
259 beneath the guide base.
260 Eight holes were drilled at site C0013 (A to H). Due to their close proximity, core from
261 these holes exhibit a broadly consistent vertical distribution (**Fig. 2a**). From 0 to ~4 mbsf
262 moderately hydrothermally altered sulfidic sediment was recovered from several holes,
263 characterized by detrital sulfide (sphalerite-pyrite-covellite), sulfate (anhydrite-barite),
264 kaolinite-muscovite (confirmed by XRD) and locally, native sulfur. Native sulfur occurs as
265 veinlets, cements (**Fig. 3c**), and coatings in voids (**Fig. 3d**). Rapid lateral and vertical variations
266 in the composition and grain size of the sulfidic sediments suggest they originated locally,
267 probably from the breakdown of nearby hydrothermal mounds and/or chimney structures. Thin
268 horizons (~10 cm) can exceed 50% sulfide (e.g. C0013E). Covellite is much less abundant than
269 sphalerite and pyrite (**Fig. 4e-f**), and framboidal pyrite was also observed (**Fig. 4g-h**). The
270 sediment is commonly poorly sorted, medium- to coarse-grained, and contains anhydrite
271 crystal fragments and lesser barite. Anhydrite shows evidence for incipient dissolution and
272 replacement by gypsum (**Fig. 4i**). SEM analysis also identified galena and tetrahedrite-
273 tennantite intergrowths with sphalerite, and an unknown silver arsenide phase associated with
274 opaline silica (**Fig. 4j**). Underlying pale grey to white sediments (from ~4 to ~5.5 mbsf) are
275 characterized by an assemblage of kaolinite-muscovite-anhydrite, with trace fine-grained
276 disseminated pyrite.
277 From ~5.5 to ~26 mbsf, site C0013 is dominated by pale bluish-grey to white mottled
278 hydrothermal clay. Mg-chlorite (clinochlore) was identified as the main alteration mineral by
279 XRD, and occurs with coarse (4-5 cm) rounded nodules of brecciated, drilling-disturbed veins
280 of white, opaque, anhydrite ± dolomite ± talc ± calcite ± quartz ± sphalerite ± pyrite (**Fig. 3a**),
281 which show evidence for erosion. Fine-grained disseminated pyrite and sphalerite are present
282 in low abundances (<1%), and rare irregular veins of anhydrite-sulfide and quartz-sulfide cut
283 the Mg-chlorite altered sediments.
284 Quartz and Mg-chlorite altered volcanic basement was recovered from below ~26 mbsf
285 in holes C0013D and C0013E (**Fig. 3b**). The rocks are unique in their hardness and distinct
286 quartz stockwork veining (most of which are barren of sulfides). Petrographic analysis has
287 revealed that ~40% of the rock is composed of volcanic glass, with the remainder devitrified
288 and replaced by quartz-chlorite and minor biotite. Rare mineralized quartz veins contain
289 sphalerite, pyrite, covellite, and in one interval, fine intergrowths of native copper and organic
290 carbon (**Fig. 3e**). Overlapping the zones of kaolinite and Mg-chlorite alteration, abundant 1-2
291 cm euhedral anhydrite crystals occur in the core (**Fig. 2a**).

292

293 **Site C0014 (distal alteration and mineralization):**

294 Site C0014 is located 350 m east of site C0013 (**Fig. 1c**) and
295 ~450 m from the NBC hydrothermal mound. A distinct colony of clams and a rocky seafloor
296 characterize the site (Takai et al., 2012). Seven holes were drilled to a maximum depth of 136.7
297 mbsf (hole C0014G; **Fig. 2b**). Compared to the two sites described above, site C0014 is
298 dominated by lower temperature alteration assemblages and is only weakly mineralized (**Fig.**
299 **2b**). From 0 to 8-10 mbsf, hemipelagic ooze and pumiceous volcaniclastic sediments exhibit
300 little evidence of hydrothermal alteration (except weak oxidation in holes C0014F and
301 C0014G), with quartz, muscovite and calcite the most abundant phases determined by XRD.
302 Sulfides commonly occur as fine-grained disseminated and framboidal pyrite grains. An
303 underlying zone of pale grey mottled clay is characterized dominated by quartz-muscovite and
304 alteration minerals illite-montmorillonite with lesser kaolinite.

305 Below ~25-30 mbsf (to the maximum depth of 136.7m; hole C0014G) Mg-chlorite
306 becomes an important alteration phase irrespective of lithology (**Fig. 2b**). Unlike at site C0013,
307 detrital muscovite and quartz persist. Anhydrite is present, but is significantly less abundant
308 with only mm-scale irregular veinlets, with halite below 57 mbsf. After casing and capping,
309 diffuse hydrothermal fluids were observed by ROV, discharging from the seafloor through the
310 space between the wall of the hole and the casing pipe (Takai et al., 2012). Thermoseal strips
311 indicated the diffusing fluids were >240 °C (Takai et al., 2012).

312 In the illite-montmorillonite and Mg-chlorite zones little sulfide mineralization was
313 observed. Pyrite occurs in trace amounts disseminated throughout the core (**Fig. 4k**) and very
314 rarely as coarser veins (with sphalerite-galena-chalcopyrite; **Fig. 4l**). XRD analysis also
315 identified covellite in some sections of core, although none was identified under binocular
316 microscope.

317

318 **Site C0015**

319 Site C0015 is located ~600 m northwest of NBC (**Fig. 1b**). Hole C0015C was the deepest
320 at the site, drilled to only 9.4 mbsf. No hydrothermal alteration was observed. Evidence for
321 weak oxidation in the uppermost layers included orange to brown iron oxide staining on pumice
322 fragments. The area is characterized by a low surface temperature gradient of 1 °C/m (Takai et
323 al., 2012). Together with the presence of iron oxides and characteristic major element
324 compositions of interstitial water samples close to those of seawater, the relatively low

temperature gradient suggests that the site represents a background site, unrelated to the hydrothermal system (Takai et al., 2012).

Site C0017 (a distal recharge site)

Site C0017 is located ~1.6 km east of North Big Chimney (**Fig. 1b**) and is characterized by extremely low heat flow, with a surface thermal gradient an order of magnitude lower than the average non-hydrothermal, trough-filling sediments of the middle Okinawa Trough (Takai et al., 2012). Hole C0017D was the deepest (150.6 mbsf) across all sites during IODP Expedition 331, recording a temperature of only 90 ± 5 °C at the base of the hole. Sediment types encountered were homogeneous hemipelagic mud, pumiceous sediment, and volcaniclastic-pumiceous breccia and mixed sand with erosional bases. No alteration was observed except weak to moderate oxidation, which was reflected in a yellow to brownish colouration in sediments, orange to brown iron oxide staining on pumice fragments, and 1-2 mm botryoidal aggregates of Fe-Si oxyhydroxides. Geochemical results, including reversals in alkalinity, ammonium and phosphate pore water concentrations, combined with downhole temperature measurements, indicate that this oxidized zone resulted from cold seawater influx (Takai et al., 2011, 2012). Notably, sulfides were absent at shallow depths, with trace pyrite consistently present below 94 mbsf.

5.2 Texture analysis

EBSD analysis was performed as it reveals information on crystal orientation, grain boundaries and phase distribution (Prior et al., 1999). EBSD data may be used to understand the controlling mineralization processes and determine any subsequent modification. Three samples were analysed, all from site C0016 - two samples of sphalerite-rich semi-massive sulfides (16B-2, 16B-3; **Fig. 3f**- blocks 2 and 3 respectively) and a quartz-chlorite altered volcanic rock with stringer and disseminated sulfides (16B-9; **Fig. 3** – block 9). For both samples of semi-massive sulfide, two areas were analysed (denoted by A and B).

For EBSD analysis, the interface between two grains is termed the grain boundary. Where the minimum misorientation angle is >10° these are termed high angle grain boundaries (HAGBs) (Halfpenny et al., 2012). Low angle grain boundaries (LAGBs) or sub-grain boundaries have misorientation angles of <10° and are composed of an array of dislocations (Halfpenny et al., 2006; Trimby et al., 1998). LAGBs represent intra-grain variations due to modification of the grains post-mineralization. There are some special orientations where there is a relationship between the lattices on either side of a boundary. One such structure is a

coincident site lattice (CSL), which describes the number of atoms that are shared on the boundary between the grains. For coherent twin boundaries Σ3, one in three atoms is shared. If the crystallographic orientations of an individual phase are fully random, then there is no distinct texture. However, in some geological systems grains can align due to mineralization and deformation processes producing a crystallographic preferred orientation (CPO) (Halfpenny, 2011; Halfpenny and Prior, 2009). If a CPO is identified it may be used to interpret the underlying processes which caused grain alignment (Fougerouse et al., 2016a; Fougerouse et al., 2016b).

Sample 16B-2 is dominated by sphalerite, with lesser pyrite, chalcopyrite, quartz, chlorite and graphite. Two areas within this sample were analysed - 16B-2A (**Fig. 5a-c**) and 16B-2B (**Fig. 5d-f**). In the prior, sphalerite exhibits a variable grain size with the grain diameter varying from 10-20µm. The sphalerite exhibits Σ3 (60°±5° about <111>) CSLs (red lines) and very little substructure development as there are few LAGBs (white lines) (**Fig. 5c**). None of the indexed phases in area 16B-2A exhibit a CPO. In area 16B-2B, the sphalerite exhibits a coarser grain size with a maximum of grain diameter of 47 µm. Sphalerite grains contain multiple Σ3 CSL's (**Fig. 5f**). All phases measured show little to no internal deformation (no LAGBs) and no CPO has been developed.

Sample 16B-3 contains sphalerite as the main phase with quartz, chlorite, pyrite, chalcopyrite, anhydrite and minor amounts of graphite (**Fig. 5g-l**). In area 16B-3A, the sphalerite is coarse grained, contains Σ3 CSLs and some of the sphalerite grains exhibit lobate grain boundaries (**Fig. 5i**). In area 16B-3B, the sphalerite is extremely coarse grained and exhibits lobate grain boundaries (**Fig. 5j & k**). There is a small area which contains finer grained sphalerite and pyrite crystals (**Fig. 5l**). None of the indexed phases in sample 16B-3 exhibit a CPO or internal deformation (**Fig. 5l**).

Sample 16B-9 is from a pyrite vein and the mineralogy is dominantly pyrite and quartz with some chlorite (**Fig. 5m & n**). The pyrite exhibits a bimodal grain size distribution between coarse (>40 µm in diameter) and fine grains (<40 µm in diameter). The quartz crystals range from euhedral to anhedral, but all grains exhibit little to no internal deformation (**Fig. 5o**). No CPO is observed.

5.3. Whole rock geochemistry

Massive sulfide from site C0016B (sample IN01) contains high concentrations of Zn (30.2%), Pb (12.3%) and Cu (2.68%), and elevated Mo (35.4 ppm), Ag (33.1 ppm), Sb (25.6 ppm) and Au (0.07 ppm) with respect to unmineralized samples from Iheya North. Low

393 concentrations of lithophile elements, such as SiO_2 (4.9 wt.%), Al_2O_3 (0.21 wt.%), MgO (0.28
394 wt.%) and K_2O (0.11 wt.%), are consistent with large mass gains of Fe, S and base metals (see
395 following section). Underlying felsic rocks (**Fig. 6a**) from site C0016 contain significantly
396 lower levels of Fe, Zn, Cu, Pb, Sb, Mo, Ag and Au (**Table 1**). Increasing MgO, Cu/Zn and
397 Fe/Zn occur down hole in C0016B. MgO values are low (0.3 wt.%) in massive sulfides (IN01),
398 ~1.0 wt.% in underlying silicified volcanic rocks (IN02-IN04), and 5.2-5.8 wt.% in quartz-
399 chlorite altered rocks at depth (IN05-IN06). Quartz-chlorite altered rocks are also characterized
400 by much higher Fe/Zn (917-1044) and Cu/Zn ratios (0.5-0.6) than overlying lithologies (<6.0
401 Fe/Zn and <0.1 Cu/Zn). SiO_2, K_2O, sulfide and sulfate concentrations are erratic down hole
402 C0016B due to varying degrees of silicification, sulfide mineralization and anhydrite veining.
403 Na_2O concentrations are consistently ~0.1 wt.% throughout, indicative of extensive feldspar
404 destruction or an absence of albite in the rhyolitic precursor. On the Box Plot of Large et al.
405 (2001a; see figure caption for description), samples from C0016B plot on a chlorite-pyrite-
406 (sericite) trend, away from the least altered dacite field, characterized by high CCPI
407 (Carbonate-chlorite-pyrite Index) and Alteration Index values (**Fig. 6b**).
408 Samples from site C0013 are in many respects geochemically similar to those from site
409 C0016 (**Table 1**). A sample of coarse grained sulfidic sediment from C0013 (IN13) is
410 characterized by high Zn (43.2%), Fe_2O_3 (9.6%), Cu (5.4%), Pb (4.4%), As (1.5%), Ag (42
411 ppm), Cd (980 ppm) Sb (104 ppm) and Mo (59 ppm). This is consistent with the presence of
412 abundant coarse sphalerite (overgrown by pyrite), covellite (**Fig. 4e**) and chalcopyrite
413 identified under binocular microscope in near surface sulfidic sediments. Galena and sulfosalts,
414 including tetrahedrite-tennantite, were identified by SEM and are intergrown with sphalerite.
415 High concentrations of Zn (3.46%) and Cu (1.89%) also occur in samples with visible sulfide
416 veining at depth (e.g. sample IN16). SiO_2, K_2O, MgO, Fe_2O_3, Na_2O, S and base metal
417 concentrations are erratic throughout the sampled sections. Samples from C0013 with
418 significant anhydrite are characterized by high CCPI and low Alteration Index values near the
419 calcite mineral node of the Box Plot (**Fig. 6b**).
420 Zinc concentrations from the relatively distal site C0014 (to 0.01% Zn) are consistently
421 lower than at sites C0013 and C0016. Hydrothermal alteration at C0014 is dominated by quartz
422 and muscovite with minor kaolinite, illite/montmorillonite, and Mg-chlorite at depth. This is
423 reflected by varying concentrations of SiO_2, K_2O, Na_2O, CaO, MgO and Al_2O_3. Na_2O
424 concentrations are significantly higher (0.3-0.92 wt.%) than at proximal sites C0013 and
425 C0016. Iron and base metal concentrations are low in all samples (<4.47 wt.% Fe_2O_3 and
426 <0.02% Cu+Pb+Zn) due to the lack of sulfides. Discounting rare anhydrite-rich units, samples

from C0014 are characterized by high Alteration Index and moderate CCPI values, typical of a distal sericite-chlorite-pyrite trend (Large et al., 2001a; **Fig. 6b**). At site C0014, Sb concentrations reach a maximum of ~7.1 ppm, which are significantly lower than at proximal sites C0016 and C0013.

Samples of felsic pumice and clay from sites C0015 and C0017 are characterized by low MgO (0.37-0.62 wt.%), Fe_2O_3 (2.3-5.3 wt.%), LOI (<6 wt.%) and base metal concentrations (<0.04% Cu+Pb+Zn). SiO_2 concentrations for pumice samples (67.8-69.4 wt.%) are typical of unaltered felsic rocks. All three samples analysed plot within the least altered dacite and rhyolite fields on the Box Plot of Large et al. (2001a) (**Fig. 6b**), containing low concentrations of Au, Ag, Bi, Cu, Mo, Pb, Sb, Te, Tl and Zn (**Table 1**).

Immobile element geochemistry: Most lithologies sampled from Iheya North are of felsic composition (**Fig. 6a**), characterized by high Zr/TiO_2 ratios. Three clay-rich samples plot closer to the intermediate field of Pearce (1996), along with massive sulfides from C0016B. These include one sample of hemipelagic clay (IN08), and two samples dominated by illite/montmorillonite (IN19, IN20). Felsic lithologies (both pumiceous volcaniclastic sediments and coherent volcanic basement) are of FII to FIIIa affinity according to the VHMS fertility diagrams of Lesher et al. (1986) and Hart et al. (2004) (**Fig. 6c**); and straddle the volcanic arc and A-type fields of Pearce et al. (1984; **Fig. 6d**). This latter diagram is shown simply to highlight the HFSE enrichment of the felsic rocks (after Piercey, 2011). With increasing mass gain at sites C0016, C0013 and C0014, Nb and Y concentrations will be diluted at a constant ratio as both elements are immobile (see arrow in **Fig. 6d**). All samples analysed herein display prominent negative Eu anomalies on chondrite-normalized REE diagrams, with slightly elevated LREE concentrations and flattish HREE profiles (**Fig. 6e**). Elevated HFSE concentrations (e.g. **Fig. 6d**), and Sc/V and Sc/TiO_2 ratios, are consistent with felsic rocks associated with VHMS deposits in ensialic settings worldwide (see Piercey, 2011; Hollis et al. 2015 and references therein).

Mass change: Mass change values were calculated for selected samples from across the Iheya North hydrothermal field using the isocon method of Grant (1986, 2004). Isocons were fitted using a range of immobile elements: Al, Ga, Hf, La, Nb, P, Ta, Tb, Ti, Th, Y, Yb, Zr (**Figure 7**). Element concentrations are scaled for plotting convenience using the values listed in **Table 2**. Sample IN07 (grey woody pumice) from site C0017 was used for a least altered composition, consistent with shipboard XRD and petrographic analysis. Although this pumice may have

been introduced from elsewhere, its similar Zr/TiO_2, Nb/Y, La/Yb_{CN} and Zr/Y ratios (**Fig. 6**) suggest it is of similar composition to the altered felsic volcanic/volcaniclastic rocks of sites C0016, C0013 and C0014. Calculated mass change values are illustrated in **Figure 8** and provided in **Table 3**. Mineralized and hydrothermally altered samples from sites C0016, C0014 and C0013 show significant mass gains in Cu-Pb-Zn-Fe-S-Au-Ag-As-Sb-Bi-Mo-Sr-Sn-Te-Tl-Mg-LOI±Si±Ca and losses of Na-K-Cs-Eu-Rb±Ba (**Fig. 8**). Mass change is most pronounced in the massive sulfides from site C0016, with large gains of Fe, S, Cu, Pb, Zn and a range of trace metals (e.g. Ag, As, Mo, Sb, Te) as to be expected, decreasing downhole (samples IN01, IN02 and IN05: **Fig. 8**). Less well mineralized footwall rocks show smaller gains of Fe, S, base and trace metals. Erratic gains of Si and Mg are due to variable silicification and chloritization. Samples from more distal sites C0013 and C0015 (represented by IN15 and IN09 respectively) have lower mass gains and losses than samples from site C0016. The clustering of mobile elements around the isocon of sample IN09 (**Fig. 7**) is consistent with the unaltered nature of site C0015, with only minor losses of SiO_2, and gains of Sr and Ba (**Fig. 8**).

5.4 Mineral chemistry

Three samples from site C0016 were characterized by electron microprobe analysis: 16B-1 (sphalerite-rich massive sulfide, from 0-9 mbsf; **Figure 3f-1**), 16B1-3 (silicified and anhydrite-sulfide veined volcanic rock, from 0-9 mbsf; **Fig. 3g**), and 16B-8 (quartz-chlorite altered volcanic rock from 27-45 mbsf; **Fig. 3i**). Chlorite analyses (n=42) plot consistently within the clinochlore and penninite fields (**Fig. 9**), characterized by extremely low Fe/Fe+Mg and moderate Si. Chlorite geothermometers (MacLean and Kranidotis, 1987; Zhang and Fyfe, 1995) yield average temperature estimates of 218-235 °C for sphalerite-rich massive sulfides (sample 16B-1), and 225-241 °C for quartz-chlorite altered volcanic rock (sample 16B-8).

White mica was analysed from sample 16B1-3 (a silicified and anhydrite-sulfide veined volcanic rock from 0-9mbsf) and was not identified in the other two samples discussed above. Mg/(Fe+Mg) ratios are high 0.90-0.94 and Na/(Na+K) ratios low (0.02). Al_{iv} values of 0.94-1.01 are indicative of phengitic white mica compositions.

6. DISCUSSION

6.1 Fluid/rock interaction and active VHMS mineralization at Iheya North

The recovery of massive sphalerite-(pyrite-chalcopyrite±galena)-rich sulfides from below the seafloor at Iheya North represents an extraordinary achievement for the IODP. At site C0016,

recovered blocks of sphalerite-rich massive sulfide from the base of North Big Chimney show clear microstructural evidence of formation via a combination of surface detrital and subsurface chemical processes (**Fig. 4c**), with no subsequent deformation as highlighted by EBSD analysis (**Fig. 5**). At least two episodes of sphalerite mineralization have been recognized. Early Fe-poor sphalerite appears to be detrital in origin and occurs as 0.5 mm subhedral, slightly rounded crystals with inclusions of chalcopyrite. This generation is overgrown by pyrite (±galena), and in turn by chalcopyrite (**Fig. 4d**). A second generation of Fe-poor sphalerite most likely occurred as the system cooled, prior to final seawater influx represented by late coarse anhydrite crystals (**Fig. 4b**). This second generation includes colloform- and atoll-textured aggregates (**Fig. 4c**).

Massive sulfides are polymetallic and characterized by high Zn (30.2%), Pb (12.3%) and Cu (2.68%), plus elevated Ag (33.1 ppm) and Sb (25.6 ppm) concentrations. Low Au concentrations (maximum 0.07 ppm) may be a result of phase separation at depth, as indicated by chloride concentrations that are lower than seawater (Chiba et al., 1996) and flashing (rapid boiling) during IODP drilling (Takai et al., 2011). This is consistent with the lower confining pressures from shallower water depths of the middle Okinawa Trough (<1000 m; Chiba, 1997) when compared to the PACMANUS (~1650 m) and DESMOS (~2000 m) systems of the Manus Basin, and similar hydrothermal fields of the Lau Basin (e.g. Valu Fa Ridge, ~1700 m) (Ishibashi and Urabe, 1995).

Altered volcanic rocks at site C0016 beneath massive sulfides exhibit quartz-muscovite/illite and quartz-Mg-chlorite alteration (**Fig. 10**), reminiscent of the proximal footwall alteration typically associated with ancient VHMS deposits (Large et al., 2001a,b; Piercey, 2009). Low concentrations of SiO_2, Al_2O_3, MgO and K_2O in massive sulfides resulted from large mass gains of Fe, S and base metals (**Fig. 8**).

At site C0013, a likely location of recent high temperature discharge, intense hydrothermal alteration obliterates primary mineralogy and texture. Near surface alteration is dominated by kaolinite and muscovite with locally abundant native S, which is indicative of the presence of acidic fluids. The entire sequence grades to Mg-chlorite dominated assemblages at depths of >5 mbsf (**Fig. 10**). Coarse-grained surficial sulfidic sediments at site C0013 contain ~43.2% Zn, 4.4% Pb, 5.4% Cu and 42 ppm Ag, with high concentrations of As, Cd, Mo, Sb and W. These sediments are interpreted to represent collapsed chimney structures. They contain significantly higher Zn, Cu, Ag, Sb and As concentrations than massive sulfides from hole C0016B.

Distinctive white coarse rounded nodules of anhydrite±dolomite±talc±calcite±quartz± sphalerite±pyrite (**Fig. 3a**) likely precipitated from down welling seawater at an early stage in the evolution of the hydrothermal system (**Fig. 11a**). These anhydrite veins were subsequently reworked during the main phase of hydrothermal activity (**Fig. 11b**). The presence of yellow native sulfur cement in the top of hole C0013E (**Fig. 3c**) indicates that the sediment was infiltrated by liquid native sulfur at temperatures between 112 and 119 °C (Takai et al., 2011). The transition from kaolinite-muscovite to chlorite-rich alteration assemblages with increasing depth (**Fig. 11b**) is similar to the gradation from paragonitized to chloritized rocks below the TAG hydrothermal field. The major difference in mineralogy between these two fields is due to lack of Fe in the system and abundance of K available from the leaching of underlying felsic basement. A zone of coarse-grained crystalline anhydrite that overlaps the kaolinite and Mg-chlorite alteration zones is interpreted to have precipitated from down welling seawater that penetrated the sediments when hydrothermal activity at the site waned (**Fig. 11c**). Volcanic basement at site C0013 consists of hard quartz and Mg-chlorite altered volcanic breccia with scattered quartz-sulfide (sphalerite-pyrite±covellite±native Cu) veining and trace fine disseminated pyrite within clasts.

6.2. Distal hydrothermal alteration, mineralization and system recharge

Site C0014 represents a more distal locality to the main zone of hydrothermal activity, ~450 m from NBC and ~350 m from site C0013 (**Fig. 10**). At site C0014, covellite and sphalerite mineralization is significantly less abundant. Anhydrite is present from ~57 mbsf as mm-scale irregular veinlets, but is in much lower abundance than at proximal site C0013. Pyrite occurs only in trace amounts and is rarely present as coarser veins. Mg-chlorite alteration occurs from ~30 mbsf, at much greater depths than sites C0016 and C0013. Higher Na_2O concentrations at site C0014 and lower Sb contents than site C0013 are consistent with the more distal location of site C0014 (e.g. Large et al., 2001b; Piercey, 2009).

Recovered lithologies from distal sites C0015 and C0017 are unaltered, with low MgO, Fe_2O_3, LOI, CCPI, AI, base metal concentrations and VHMS 'pathfinder' elements (e.g. Sb, Sn, Cd, Tl; Large et al., 2001b; Piercey, 2009). Downhole temperature profiles at C0017 are also indicative of lateral fluid flow recharge into the system approximately 1.6 km east of NBC (Takai et al., 2011). Site C0015 is interpreted to represent a background locality where porous strata are saturated with seawater.

6.3. A modern analogue for Kuroko-type VHMS mineralization

Recent interest surrounding the potential to mine modern seafloor massive sulfide (SMS) deposits, such as the Solwara 1 deposit of the Manus Basin (Golder Associates, 2012; Yeats, 2012), has highlighted the importance of identifying robust modern analogues for different styles of VHMS mineralization. For instance, the Cu-Zn rich TAG site, a sediment-starved system on the Mid Atlantic Ridge (e.g. ODP Expedition 158), has been compared to Cyprus-type VHMS deposits (Hannington et al., 1998). IODP Expedition 331 was the first time an active hydrothermal system in a continental back-arc setting has been drilled by the ODP / IODP (Takai et al., 2011, 2012). VHMS deposits which form in these settings fall into the Kuroko-type class (Barrie and Hannington, 1999; Galley et al., 2007; Piercey, 2011).

Kuroko-type VHMS deposits are typically polymetallic (Zn-Pb-Cu-Ag-Au), of high grade (Piercey, 2007), and hosted in bimodal felsic flow-dominated sequences where felsic rocks are in greater abundance than mafic rocks and there are less than 15% of siliciclastic rocks in the host succession (Galley et al., 2007; Piercey, 2011). On idealized cross sections, Kuroko-type VHMS deposits are developed on felsic flow complexes, such as rhyolite domes with associated tuffs and breccias (Franklin, 1981). Eight zones of massive/semi-massive mineralization were recognized by Eldridge et al. (1983) which may be present, and three zones associated with the underlying chloritic stockwork. In descending order from the top of the deposit the massive zones are: i) tetsusekiei (quartz-hematite±barite±sulfide), ii) barite ore (barite>sulfide), iii) massive black ore (sphalerite±barite>pyrite-galena>tetrahedrite); iv) semi-massive black ore (sphalerite±barite>pyrite>chalcopyrite-quartz), v) massive yellow ore (chalcopyrite-pyrite>quartz); vi) powdery yellow ore (pyrite>chalcopyrite); vii) massive pyrite ore (pyrite>>chalcopyrite>>sphalerite), and viii) massive gypsum-anhydrite ore (Ca sulfates>>sulfides). These zonations typically occur within a broadly stratiform mound, with the first seven forming imperfectly concentric shells, often with gradational contacts (unless reworked) (Eldridge et al., 1983). An underlying discordant zone of siliceous ore is often associated with the underlying chloritic stockwork with a general zonation from yellow ore (quartz>pyrite>chalcopyrite) in the middle, toward a more sphalerite-galena rich mineral assemblage at the base of the overlying lens, and a quartz>pyrite>>chalcopyrite mineralogy at depth (Eldridge et al., 1983). Classic examples of Kuroko-type VHMS deposits are found in the Honshu arc of Japan in the Hokuroku district, with deposit clusters associated with back-arc rifting (Yamada and Yoshida, 2011), the Mount Read volcanic belt of SE Australia (Large et al., 2001b), Buchans Group of Newfoundland (Piercey et al., 2007), and Skellefte distict of northern Sweden (Allen et al., 1996).

At Iheya North, massive sulfides intercepted at the base of North Big Chimney strongly resemble the black ore of the Miocene-age Kuroko deposits of Japan (Sato, 1974, 1977), with equivalents to the yellow, gypsum and siliceous ores also recogized by Ishibashi et al. (2013). Massive sulfides are polymetallic and characterized by high Zn (30.2%), Pb (12.3%) and Cu (2.68%), and elevated Ag (33.1 ppm) and Sb (25.6 ppm) concentrations. These metal concentrations are consistent with massive sulfides from Kuroko-type VHMS deposits worldwide (e.g. Barrie and Hannington, 1999; Galley et al., 2007; Large et al., 2001b; Piercey, 2007, 2009), in addition to the increased abundance of pyrite with respect to sphalerite at depth - both on the local scale within the massive sulfide and overall in the sequence (e.g. Sato, 1977; Eldridge et al., 1983). This is also reflected by higher Fe/Zn ratios with depth at site C0016. The clastic nature of the massive and semi-massive sulfides at site C0016 is also consistent with observations from the Kuroko deposits of Japan (e.g. Kuroda, 1977; Eldridge et al., 1983).

The quartz-Mg-chlorite basement present at sites C0016, C0013 and C0014 is typical of high-temperature hydrothermal alteration associated with VHMS systems (Galley et al., 2007; Piercey, 2009). All rocks analysed from C0016 show large gains in SiO_2 and MgO, with the latter increasing downhole (**Fig. 8**). It is important to note the reduced depth of the Mg-chlorite alteration towards NBC - from ~30 mbsf at site C0014 to ~6 mbsf at site C0013 (**Fig. 10**). Aoyama et al. (2014) highlight that this zone at site C0014 corresponds with shifts in Mg, K and SO_4 pore water chemistry and $\delta^{34}S$ values. Whereas the unaltered sediment at site C0014 (**Fig 2b**) is saturated with seawater, the Mg-chlorite altered zone is dominated by hydrothermal fluid and has yielded significantly higher temperatures (Takai et al., 2011). Bacteriogenic sulfate reduction is only evident in the unaltered sediments (Aoyama et al., 2014).

Decreasing Na_2O concentrations in felsic volcanic and volcaniclastic rocks at Iheya North with proximity to NBC is consistent with observations from ancient Kuroko-type VHMS deposits (Date et al., 1983; Hashiguchi et al., 1983; Piercey, 2009). For example, Date et al. (1983) recognized a Na_2O-depleted dacite mass with the lateral dimensions of 1.5 by 3 km immediately below the ore horizon associated with the Fukazawa deposits. This was interpreted to reflect feldspar destruction and sericite formation at relatively low pH and high temperatures. It was hypothesised that much of the sodium lost from footwall lithologies was added to the rocks in zones I (distal; forming analcime) and IV (proximal; forming Na-montmorillonite in the hanging-wall). In the Miocene footwall rocks of the Uwamuki deposits, Urabe et al. (1983) noted a mineralogical zonation from core to margin of quartz-sericite, sericite-chlorite-quartz, remnant albite-sericite-chlorite-quartz and kaolinite-quartz-sericite-chlorite±albite.

627 Recovered footwall felsic volcanic rocks from site C0016 (and elsewhere) are of FII to
628 FIII affinity with well-developed negative Eu anomalies, similar to felsic volcanic rocks
629 hosting ancient Kuroko-type VHMS deposits that formed in Phanerozoic ensialic back-arc
630 settings worldwide (e.g. Leat et al., 1986; McConnell et al., 1991; Piercey, 2011). In some
631 instances the period of VHMS mineralization may be associated with a shift in immobile
632 element characteristics of the host lithologies (i.e. higher HFSE concentrations in pre-ore felsic
633 rocks; Yamada and Yoshida, 2011). However, this features has also been observed in bimodal-
634 mafic or Noranda-type VHMS systems (e.g. Golden Grove & Teutonic Bore; Hollis et al.,
635 2015).
636 Chlorite analyses from site C0016 plot consistently within the Mg-rich clinochlore and
637 penninite fields (**Fig. 9**). These compositions are similar to chlorite associated with the SE
638 Australian Kuroko-type VHMS deposits such as Thalanga, and some analyses of footwall
639 chlorite at Hellyer (**Fig. 9**). Fe/Fe+Mg ratios from Iheya North are significantly lower than
640 values reported at other active hydrothermal fields such as TAG and PACMANUS, plus
641 Noranda-type (i.e. bimodal-mafic) VHMS deposits (e.g. Noranda belt, Mattagami Lake; **Fig.**
642 **9**). Work by McLeod and Stanton (1984) on the SE Australian Kuroko-type VHMS deposits
643 (e.g. Woodlawn, Que River) observed that chlorite associated with sphalerite-rich ore had
644 significantly lower Fe/Fe+Mg ratios than chalcopyrite-rich samples. This is entirely consistent
645 with chlorite geothermometers which utilise Fe/Fe+Mg ratios (e.g. MacLean and Kranidotis,
646 1987), as higher temperatures would be expected for chalcopyrite precipitation. Fe-poor
647 sphalerite and Mg-rich chlorite compositions at Iheya North are consistent with the overall low
648 Fe-budget of the system, and Zn-rich nature of the mineralization.
649 Chlorite geothermometers which utilise Fe/Fe+Mg ratios (MacLean and Kranidotis,
650 1987; Zhang and Fyfe, 1995) yield average temperature estimates of 218-235 °C for sphalerite-
651 rich massive sulfides and 225-241 °C for quartz-chlorite altered volcanic rocks characterized
652 by higher Cu/Fe and Cu/Zn ratios. These temperatures are consistent with hydrothermal fluids
653 associated with Kuroko-type VHMS mineralization (e.g. Kalogeropoulos and Scott, 1983;
654 Shikazono et al., 1983), with temperatures of >250 ˚C when associated with chalcopyrite.
655 EBSD data also reveal higher temperature microstructures downhole at site C0016, and
656 temperature induced grain boundary migration through more lobate HAGBs (e.g. 16B-3B, **Fig.**
657 **5l**).
658
659 **6.4. Role of sediments on fluid flow and chemistry**

660 Although there is less interaction between hydrothermal fluids and sediments at Iheya North
661 than the JADE and CLAM sites of the middle Okinawa Trough (Glasby and Notsu, 2003), high
662 alkalinity, NH_4^+, CH_4 and CO_2 at Iheya North are still indicative of some reaction with organic
663 matter. Anomalously high alkalinity and NH_4^+ at the CLAM site of the middle Okinawa
664 Trough, coupled with significantly higher $\delta^{34}S$ of sulfate than ambient seawater indicate that
665 sulfate reduction plays a dominant role in decomposing organic material (see Glasby and
666 Notsu, 2003). Oxidation of significant quantities of H_2S in organic matter at Iheya North,
667 evident from the local presence of native S, coupled with Mg-fixation in chlorite ultimately
668 resulted in the stabilization of the potassic alteration assemblages observed during IODP
669 Expedition 331. Sediment input has also previously been used to explain higher concentrations
670 of Pb (13.5%), Zn (31.4%), Sb (1,140 ppm), As (1,730 ppm) and Ag (465 ppm) in chimney
671 samples from Iheya North (average values from Ueno et al., 2003) than in Kuroko-type
672 deposits (Glasby and Notsu, 2003). Lead in the JADE deposits is derived from both sediments
673 and volcanic rocks (Halbach et al., 1997; Zeng et al. 2000), similar to the Kuroko-type VHMS
674 deposits of Japan (Fehn et al., 1983). For comparison, the influence of sediment in mafic
675 dominated hydrothermal systems is provided by ODP legs to the un-sedimented TAG VHMS
676 mound and the sedimented Middle Valley (summarized by Shanks, 2012).
677 More recent work by Keith et al. (2014) has linked Fe/Zn ratios in sphalerite to the
678 influence of fS_2 and fO_2 on Fe partitioning between fluids and sphalerite. It was stated that
679 sphalerite from sediment-hosted vents has systematically higher S concentrations and Fe/Zn
680 ratios than those of the sediment-starved vents. This is again consistent with data presented by
681 Ishibashi et al. (2015) from the middle Okinawa Trough. Whereas the Iheya North, Yoron,
682 Minami-Ensei, Irabu and Hatoma fields are characterized by low Fe/Zn ratios in sphalerite
683 (FeS typically <5 mol %), data from the more sedimented JADE and Yonaguni IV fields
684 progressed to considerably higher values (Ishibashi et al., 2015). The CLAM site in particular
685 is characterized by a thick blanket of muddy sediments, with associated Zn-mineralization
686 dominated by wurtzite (Glasby and Notsu, 2003). Proton-induced X-ray emission mapping has
687 confirmed the Fe-poor nature of the sphalerite from site C0016 massive sulfides, plus an
688 association between sphalerite and high Cd (Yeats & Laird, unpublished).
689 As impermeable hemipelagic sediments are interlayered with volcaniclastic sediments
690 through the upper part of the Iheya North stratigraphy (**Fig. 2**), hydrothermal fluids are
691 channelled laterally in porous and permeable volcaniclastic units, and vertically predominantly
692 through faults (Takai et al., 2011; **Fig. 10**). Locally sourced woody pumice and pumiceous
693 pyroclastic flow deposits have been recovered by numerous gravity cores obtained from the

central valley of Iheya North Knoll (Oiwane et al., 2008). In all cores, thick pumice layers with coarse to fine grain sizes were found just below the seafloor. These layers often contain abundant gas-filled voids accompanied by elemental sulphur and sulfide minerals, deposited by a gas-rich hydrothermal fluid (Oiwane et al., 2008). Shipboard pore-water chemistry also shows clear evidence for the compartmentalization of hydrothermal fluids due to the presence of thick sequences of hemipelagic sediment (Takai et al., 2011).

7. CONCLUSIONS

The mineralization and alteration assemblages intercepted during IODP Expedition 331 at Iheya North provide a relatively complete (though fragmental) profile through a developing Kuroko-type VHMS system. At site C0016, located adjacent to the foot of the actively venting NBC massive sulfide mound, massive sphalerite-(pyrite-chalcopyrite±galena)-rich sulfides were recovered that strongly resemble the black ore of the Miocene-age Kuroko deposits of Japan. Sulfide mineralization shows clear evidence of formation through a combination of surface detrital and subsurface chemical processes, with at least some sphalerite precipitating into void space in the rock. Underlying volcanic rocks exhibit quartz-muscovite/illite and quartz-Mg-chlorite alteration reminiscent of VHMS proximal footwall hydrothermal alteration.

Site C0013, ~100 m east of NBC, represents a likely location of recent high temperature discharge, with surficial coarse-grained sulfidic sediments containing high concentrations of As, Mo, Sb and W. Near surface alteration is dominated by kaolinite and muscovite with locally abundant native sulfur, indicative of acidic fluids, grading to Mg-chlorite dominated assemblages at depths of >5 mbsf. Late coarse-grained anhydrite veining overprints earlier alteration and is interpreted to have precipitated from down welling seawater as hydrothermal activity waned. At site C0014, ~150 m farther east, hydrothermal assemblages are characterized by illite/montmorillonite, with Mg-chlorite present at ~30 mbsf. Recovered lithologies from distal, recharge site C0017 are unaltered.

The metal tenors and alteration assemblages at Iheya North are significantly different from those observed at deposits hosted in Mid Ocean Ridge (Cyprus-type) and primitive arc (e.g. Noranda-type) environments. Mineralization and alteration assemblages are consistent with the Iheya North system representing a modern analogue for Kuroko-type VHMS mineralization. Fluid flow is focussed laterally along pumiceous volcaniclastic strata (compartmentalized between impermeable hemipelagic sediments), and vertically along faults.

728 **ACKNOWLEDGEMENTS**

729 The authors thank the crew of R/V Chikyu during IODP Expedition 331, particularly co-chief
730 scientists Ken Takai and Mike Mottl. Junichiro Ishibashi, Stephen Bowden and Yuka Masaki
731 are thanked for thoughtful on-board discussions. Costs associated with Chris Yeats', Steven
732 Hollis', Juan Carlos Corona's and Gordon Southam's participation in IODP Expedition 331
733 were supported by the Australia-New Zealand IODP Consortium, IODP UK, the U.S. Science
734 Support Program, and the National Sciences and Engineering Research Council of Canada,
735 respectively. Steven Hollis is currently supported by the Irish Centre for Research in Applied
736 Geosciences (iCRAG) through funding from Science Foundation Ireland (SFI). Financial
737 support for Angela Halfpenny was provided the Commonwealth Scientific and Industrial
738 Research Organisation's (CSIRO), Office of the Chief Executive (OCE) postdoctoral research
739 funding scheme. Stephen Barnes (CSIRO) is thanked for funding whole rock geochemistry.
740 The authors thank the Integrated Ocean Drilling Program for the opportunity to sail and access
741 to samples. Marco Fiorentini acknowledges support from the Australian Research Council
742 through Linkage Project LP120100668, the Future Fellowship Scheme (FT110100241), and
743 the ARC Centre for Excellence for Core to Crust Fluid Systems (CE11E0070). Crystal
744 LaFlamme acknowledges support from the Minerals Research Institute of Western Australia
745 and Science and Industry Endowment Fund and Geological Survey of Western Australia. This
746 manuscript was greatly improved by constructive comments from editor Franco Pirajno and
747 two anonymous reviewers. This is contribution *** from the ARC Centre for Excellence for
748 Core to Crust Fluid Systems.

749

750 **LIST OF FIGURES**

751 **Figure 1. (a)** Geological Setting of the Iheya North hydrothermal field of the middle Okinawa
752 Trough, Japan (modified after Ishibashi et al., 2015; Shinjo & Kato, 2000). **(b-c)**
753 Bathymetric maps of the Iheya North hydrothermal field and IODP Expedition 331 drill
754 sites (after Ishibashi et al., 2015; Takai et al., 2011). NBC, North Big Chimney.

755 **Figure 2.** Sedimentary logs for the deepest holes at sites C0013 and C0014 with alteration
756 assemblages determined by shipboard XRD indicated. **(a)** Hole C0013E. **(b)** Hole
757 C0014G.

758 **Figure 3.** Key lithologies recovered from sites C0013 **(a-e)** and C0016 **(f-j)**. All core recovered
759 from site C0016 is shown. **(a)** Mottled Mg-chlorite and anhydrite alteration in sediments
760 from hole C0013D. Note the large white nodules of anhydrite with truncated internal
761 structures, indicating physical or chemical erosion after precipitation. **(b)** Quartz and

762 Mg-chlorite altered volcanic basement with stockwork veining (site C0013E) containing
763 sphalerite, pyrite and covellite. **(c)** Native sulfur bearing sediment at the top of hole
764 C0013E. As the sulfur occurs as veinlets and cements this implies it was liquid when the
765 interval formed. **(d)** Native S crystalline linings on gaseous or fluid filled voids in silty
766 mud from hole C0013F. **(e)** Native Cu (confirmed by SEM) and organic carbon present
767 in volcanic basement at depth from site C0013E. **(f)** Blocks of hard clastic massive/semi-
768 massive sulfide dominated by sphalerite from C0016B (labelled 1-3; from 0-9 mbsf). **(g)**
769 Silicified volcanic with sulfide veining (labelled 4) recovered from the core catcher from
770 0-9 mbsf. **(h)** Lithologies recovered from between 9 and 27 mbsf: silicified volcanic rock
771 (labelled 5), a coarsely crystalline anhydrite aggregate with sulfide veining (labelled 6)
772 and quartz-clay altered volcanic breccia (labelled 7). **(i)** Quartz-chlorite altered volcanic
773 rock recovered from between 27-45 mbsf, which displays a network of quartz-chlorite-
774 pyrite veins. **(j)** Quartz-chlorite-pyrite veining cut by a later anastomosing pyrite-
775 anhydrite vein network, in quartz-chlorite altered volcanic basement (recovered from the
776 core catcher; from 27-45 mbsf).
777 **Figure 4.** Petrographic and backscattered SEM photomicrographs of samples recovered from
778 Iheya North. **(a)** Massive sulfide from site C0016B showing intergrown pyrite-
779 chalcopyrite-sphalerite-galena (reflected light). Chalcopyrite has overgrown pyrite, with
780 sphalerite showing chalcopyrite disease. **(b)** Coarsely crystalline anhydrite overgrowing
781 quartz and sulfide in sphalerite-rich massive sulfides from site C0016B. **(c)**
782 Colloform/atoll textured sphalerite overgrowing pyrite and chalcopyrite in massive
783 sulfides at site C0016B (reflected light). **(d)** Silicified volcanic rock underlying massive
784 sulfides at site C0016B (reflected light). Sphalerite is overgrown by galena, and in turn
785 by pyrite and chalcopyrite. **(e)** Covellite present in sulfidic sediments from site C0013
786 (image taken under binocular microscope). **(f)** SEM image of euhedral covellite from
787 sulfidic sediment (near surface) at C0013E. **(g)** Euhedral and framboidal pyrite present
788 in sulfidic sediments at site C0013 (image taken under binocular microscope). **(h)** SEM
789 photomicrograph of framboidal pyrite aggregates from sulfidic sediment (near surface)
790 C0013C. **(i)** SEM photomicrograph showing the hydration of anhydrite to gypsum during
791 dissolution at site C0013B. **(j)** SEM photomicrograph of opaline silica with silver
792 arsenide (bright white material) from site C0013B. **(k)** Euhedral pyrite intergrowths in
793 clay from C0014G **(l)** SEM photomicrograph of a polymetallic sulfide vein from site
794 C0014G with intergrown sphalerite, chalcopyrite and galena.

Figure 5. (a, d, g, j, m) Reflected light photomicrographs of the areas analysed by coincident EDS/EBSD. **(b, e, h, k, n)** phase maps created from EDS data (sphalerite = dark blue, quartz = red, pyrite = orange, chalcopyrite = lime green, chlorite = aqua blue, graphite = grey, anhydrite = pink). **(c, f, i, l, o)** EBSD data plotting the phases (sphalerite = blue, quartz = red, pyrite = orange, chalcopyrite = lime green) overlain on the pattern quality map, with high angle grain boundaries (HAGB) in black, low angle grain boundaries (LAGB) in white, and sigma 3 coincident site lattices (CSL) in red. *Samples:* **Figure 5a-f:** sphalerite-rich semi-massive sulfide (C0016B, block 2 in **Figure 3f**). **Figure 5g-l:** sphalerite rich semi-massive sulfide (C0016B, block 3 in **Figure 3f**). **Figure 5m-o** quartz and Mg-chlorite altered volcanic rock with stringer sulfides (C0016B, block 9 in **Figure 3j**)

Figure 6. Whole rock geochemical variation at Iheya North. **(a)** Pearce (1996) whole rock Zr/TiO_2 vs. Nb/Y discrimination diagram for the classification of hydrothermally altered volcanic and volcaniclastic rocks. All samples plot within the felsic (rhyolite/dacite) field except for 5 samples which contain significant quantities of hemipelagic/hydrothermal clay (IN08 and IN19-20 respectively) or are strongly mineralized (IN01). **(b)** Alteration Box Plot of major element mobility (after Large et al. 2001a). CCPI (Chlorite-Carbonate-Pyrite Index) = 100 (MgO + FeO) / (MgO + FeO + Na_2O + K_2O). AI (Ishikawa Alteration Index) = 100 (K_2O + MgO) / (K_2O + MgO + Na_2O + CaO). The Ishikawa Alteration Index quantifies the intensity of sericite and chlorite alteration that occurs in footwall rocks proximal to Kuroko-type VHMS deposits. High AI is associated with the breakdown of sodic plagioclase and volcanic glass and their replacement by sericite and chlorite. The Chlorite-Carbonate-Pyrite Index quantifies increases in MgO and FeO associated with Mg-Fe chlorite development, which commonly replaces albite, K feldspar or sericite. It also is affected by Mg-Fe carbonate alteration, and enrichments in pyrite, magnetite and hematite. Mineral nodes and common alteration trends associated with hydrothermal alteration are shown. **(c)** Zr/Y vs. Y fertility plot of Lesher et al. (1986) for the VHMS prospectivity of felsic rocks. Inset image shows the La/Yb_{CN} vs. Yb_{CN} fertility plot of Hart et al. (2004). Samples analysed from Iheya North are predominantly of FII to FIIIa affinity and similar to VHMS associated felsic rocks in ensialic arc settings worldwide. **(d)** Nb vs. Y diagram highlighting the HFSE enrichment of the least altered felsic rocks at Iheya North. Large mass gains of mobile elements (e.g. Fe, S, Si, Mg, Zn) result in the dilution of Nb and Y while maintaining immobile-element ratios. **(e)** Chondrite normalized REE diagram illustrating the slight LREE enrichment, flattish

HREE profiles and pronounced negative Eu anomalies for most samples. Chondrite normalization values from McDonough and Sun, 1995).

Figure 7. Isocon diagrams for representative samples from Iheya North (after the method of Grant, 1986, 2004). Isocons were fitted using a range of immobile elements (shown in red). Element concentrations are scaled for plotting convenience using the values listed in Table 2. **(a)** IN01, sphalerite-rich massive sulfide from site C0016 (see **Figure 3a**). **(b)** IN02, silicified volcanic rock with disseminated sulfides from site C0016 that underlies massive and semi-massive sulfide (see **Figure 3f**). **(c)** IN05, quartz-Mg-chlorite altered volcanic rock with stringer sulfides from site C0016 (see **Figure 3h**). **(d)** IN15, quartz-chlorite altered volcanic rock from depth at site C0013. **(e)** IN09, unaltered pumice with trace oxidized yellow clay staining from site C0015. **(f)** Schematic cartoon for the interpretation of isochon diagrams.

Figure 8. Calculated mass change values for selected samples from sites Iheya North after Grant (1986, 2004). Mass change was calculated using the immobile element isocons and equations in **Figure 7**. Large mass gains of Zn-Pb-Cu-Fe-S occur in IN01. Underlying silicified (IN02) and quartz-chlorite altered volcanic rocks also show large gains in Si±Mg, whereas samples from C0013 (IN15) and C0015 (IN09) show significantly reduced mass gains.

Figure 9. Chlorite chemistry for samples analysed from hole C0016B compared to other active hydrothermal systems and ancient VHMS deposits. Data compiled from: Arctic VHMS deposit, Alaska (Schmidt 1988), Heath Steel B Zone VHMS deposit, New Brunswick, Canada (Lentz et al., 1997), Hellyer VHMS deposit, western Tasmania, Australia (Gemmell and Fulton, 2001), Horne VHMS deposit, Noranda, Quebec (MacLean and Hoy, 1991), Iberian Pyrite belt, SW Spain (Sánchez-España et al., 2000), Mattagami Lake, Quebec, Canada (Costa et al., 1983), PAC-MANUS (Paulick and Bach, 2006), TAG (Sturz et al., 1998), Thalanga VHMS deposit, northern Queensland, Australia (Paulick et al., 2001), Turkey VMS deposits (Catagay, 1993), Wolverine volcanic-sediment hosted deposit, Finlayson Lake, Canada (Bradshaw et al., 2008).

Figure 10. Schematic cartoon for the Iheya North hydrothermal field.

Figure 11. Schematic model for evolution of hydrothermal activity at site C0013. **(a)** Eroded anhydrite veining/nodules occur within a mixed sequence of felsic volcaniclastic rocks and hemipelagic sediments on an unaltered volcanic basement. **(b)** Hydrothermal activity is associated with the alteration of the volcanic basement to quartz-Mg-chlorite and Mg-chlorite-talc in the overlying sediments, and venting at the seafloor. The uppermost

863 portion of the sedimentary sequence is characterized by a lower temperature assemblage
864 of kaolinite-muscovite, indicative of acidic fluids. **(c)** As hydrothermal activity ceases,
865 cool seawater infiltrates the sediment precipitating coarsely crystalline anhydrite above
866 the 150 °C isotherm. Sulfide chimneys collapse to form occurrences of sulfide-rich
867 sediment, which contain varying base metal concentrations.
868
869 **REFERENCES**

870 Allen, R.L., Weihed, P., Svensson, S.A., 1996. Setting of Zn-Cu-Au-Ag massive sulphide deposits in the evolution
871 and facies architecture of a 1.9 Ga marine volcanic arc, Skellefte district, Sweden. Economic Geology, 91,
872 1022-1053.
873 Aoyama, S., Nishizawa, M., Takai, K., Ueno, Y., 2014. Microbial sulfate reduction within the Iheya North
874 subseafloor hydrothermal system constrained by quadruple sulfur isotopes. Earth and Planetary Science
875 Letters, 398, 113-126.
876 Barrie, C.T., Hannington, M.D., 1999. Introduction: classification of VMS deposits based on host rock
877 composition, in: Barrie, C.T., Hannington, M.D. (Eds.), Volcanic-associated massive sulfide deposits:
878 processes and examples in modern and ancient settings. Reviews in Economic Geology, 8, 2-10.
879 Barrie, C.T., Ludden, J.N., Green, T., 1993. Geochemistry of volcanic rocks associated with Cu-Zn and Ni-Cu
880 deposits in the Abitibi Subprovince. Economic Geology, 88, 1341-1358.
881 Barriga, F., Binns, R., Baldauf, J., Miller, D.J, 2000. Anatomy of an active, felsic-hosted hydrothermal system,
882 eastern Manus Basin. Leg 193 Scientific Prospectus, Ocean Drilling Program, 1-60.
883 Bradshaw, G.D., Rowins, S.M., Peter, J.M., Taylor, B.E., 2008. Genesis of the Wolverine volcanic sediment-
884 hosted massive sulfide deposit, Finlayson Lake District, Yukon, Canada: mineralogical, mineral chemical,
885 fluid inclusion, and sulfur isotope evidence. Economic Geology, 103, 35-60.
886 Catagay, M.N., 1993. Hydrothermal alteration associated with volcanogenic massive sulfide deposits: examples
887 from Turkey. Economic Geology, 88, 606-621.
888 Chiba, H., Ishibashi, J.-I., Ueno, H., Oomori, T., Uchiyama, N., Takeda, T., Takemine, C., Ri, J., Itomitsu, A.,
889 1996. Seafloor hydrothermal systems at North Knoll, Iheya Ridge, Okinawa Trough. JAMSTEC Journal of
890 Deep Sea Research, 12, 211-219. (in Japanese with English Abstract)
891 Chiba, H., 1997. Geochemistry of active hydrothermal systems in Okinawa Trough back arc basin. JAMSTEC
892 Deep-Sea Research, Special Volume, 63-68.
893 Connelly, D.P., Copley, J.T., Murton, B.J., Standfield, K., Tyler, P.A., German, C.R., Van Dover, C.L., Amon,
894 D., Furlong, M., Grindlay, N., Hayman, N., Hühnerbach, V., Judge, M., Le Bas, T., McPhial, S., Meier, A.,
895 Nakamura, K.-i., Nye, V., Pebody, M., Pedersen, R.B., Plouviez, S., Sands, C., Searle, R.C., Stevenson, P.,
896 Taws, S., Wilcox, S., 2012. Hydrothermal vent fields and chemosynthetic biota on the world's deepest seafloor
897 spreading centre. Nature Communications, 3, 620.
898 Costa, U.R., Barnett, R.L., Kerrich, R., 1983. The Mattagami Lake mine Archean Zn-Cu sulfide deposit, Quebec:
899 hydrothermal coprecipitation of talc and sulfides in a sea-floor brine pool – evidence from geochemistry,
900 $^{18}O/^{16}O$, and mineral chemistry. Economic Geology, 78, 1144-1203.

Date, J., Watanabe, Y., Saeki, Y., 1983. Zonal alteration around the Fukazawa Kuroko deposits, Akita Prefecture, northern Japan. In: Ohmoto, H., Skinner, B.J. (eds.) Kuroko and related volcanogenic massive sulfide deposits. Economic Geology, Monograph 5, 365-386.

de Ronde, C.E.J., Faure, K., Bray, C.J., Chappell, D.A., Wright, I.C., 2003. Hydrothermal fluids associated with seafloor mineralization at two southern Kermadec arc volcanoes, offshore New Zealand. Mineralium Deposita, 38, 217-233.

de Ronde, C.E.J., Hannington, M.D., Stoffers, P., Wright, I.C., Ditchburn, R.G., Reyes, A.G., Ishibashi, J., Lebon, G.T., Bray, C.J., Resing, J.A., 2005. Evolution of a submarine magmatic-hydrothermal system: Brothers volcano, southern Kermadec arc, New Zealand. Economic Geology, 100, 1097-1133.

Eldridge, C.S., Barton Jr, P.B., Ohmoto, H., 1983. Mineral textures and their bearing on the formation of Kuroko orebodies. In: Ohmoto, H., Skinner, B.J. (eds.) Kuroko and related volcanogenic massive sulfide deposits. Economic Geology, Monograph 5, 241-281.

Fehn, U., Doe, B.R., Delevaux, M.H., 1983. The distribution of lead isotopes and the origin of Kuroko ore deposits in the Hokuroku district, Japan. Economic Geology Monograph 4, 488-506.

Fougerouse, D., Micklethwaite, S., Halfpenny, A., Reddy, S.M., Cliff, J.B., Martin, L.A.J., Kilburn, M., Guagliardo, P., Ulrich, S., 2016a. The golden ark: Arsenopyrite crystal plasticity and the retention of gold through high strain and metamorphism. Terra Nova, 28, 181-187.

Fougerouse, D., Micklethwaimte, S., Tomkins, A.G., Mei, Y., Kilburn, M., Guagliardo, P., Fisher, L.A., Halfpenny, A., Gee, M., Paterson, D., Howard, D.L., 2016b. Gold remobilisation and formation of high grade ore shoots driven by dissolution-reprecipitation replacement and Ni substitution into auriferous arsenopyrite. Geochimica et Cosmochimica Acta, 178, 143-159.

Fouquet, Y., Zierenberg, R., Miller, J., the Leg 169 Scientific Party, 1997. Leg 169 drills a major massive sulfide deposit on a sediment-buried spreading center. JOIDES Journal, 23, 4–5.

Franklin, J.M., Sangster, D.F., Lydon, J.W., 1981. Volcanic-associated massive sulfide deposits. Economic Geology, 75th Anniversary Volume, 485-627.

Franklin, J.M., Gibson, H.L., Galley, A.G., Jonasson, I.R., 2005. Volcanogenic massive sulfide deposits, in: Hedenquist, J.W., Thompson, J.F.H., Goldfarb, R.J., Richards, J.P. (Eds.), Economic Geology 100th Anniversary Volume. Society of Economic Geologists, 523-560.

Galley, A.G., Bailes, A.H., Kitzler, G., 1993. Geological setting and hydrothermal evolution of the Chisel Lake and North Chisel Zn-Pb-Cu-Ag-Au massive sulfide deposits, Snow Lake, Manitoba. Exploration and Mining Geology, 2, 271-295.

Gemmell, J.B., Fulton, R., 2001. Geology, genesis, and exploration implications of the footwall and hanging-wall alteration associated with the Hellyer volcanic-hosted massive sulfide deposit, Tasmania, Australia. Economic Geology, 96, 1003-1035.

Glasby, G.P., Lizasa, K., Hannington, M., Kubota, H., Notsu, K., 2008. Mineralogy and composition of Kuroko deposits from northeastern Honshu and their possible modern analogues from the Izu-Ogasawara (Bonin) Arc south of Japan: implications for mode of formation. Ore Geology Reviews, 34, 547-560.

Glasby, G.P., Notsu, K., 2003. Submarine hydrothermal mineralization in the Okinawa Trough, SW of Japan: an overview. Ore Geology Reviews, 23, 209-339.

940 Golder Associates., 2012. Mineral resource estimate, Solwara project, Bismark Sea, PNG: technical report
941 compiled under NI43-10, no SL01-NSG-RPT-7020-001 Rev 1, March 23, 2012, 218p.
942 Grant, J.A., 1986. The Isocon diagram – a simple solution to Gresens Equation for metasomatic alteration.
943 Economic Geology, 81, 1976-1982.
944 Grant, J.A., 2005. Isocon analysis: a brief review of the method and applications. Physics and Chemistry of the
945 Earth, 30, 997-1004.
946 Halbach, P., Pracejus, B., Märten, A., 1993. Geology and mineralogy of massive sulfide ores from the Central
947 Okinawa Trough, Japan. Economic Geology, 88, 2210-2225.
948 Halbach, P., Hansmann, W., Köppel, V., Pracejus, B., 1997. Whole-rock and sulfide lead-isotope data from the
949 hydrothermal JADE field in the Okinawa back-arc trough. Mineralium Deposita, 32, 70-78.
950 Halfpenny, A., 2010. Some important practical issues for collection and manipulation of electron backscatter
951 diffraction (EBSD) data from rocks and minerals. J. Vir. Exp. 35, 1-18.
952 Halfpenny, A., 2011. Application of EBSD to Oceanic Gabbros: Insights into an Oceanic Core complex, Australian
953 Microscopy & Microanalysis Newsletter, 42-44.
954 Halfpenny, A., Hough, R.M., Verrall, M., 2013. Preparation of samples with both hard and soft phases for electron
955 backscatter diffraction: Examples from gold mineralization. Microsc. Microanal. 19, 1007-1018.
956 Halfpenny, A., Prior, D.J., 2009. An electron backscatter diffraction study of a gabbroic shear zone, IODP
957 Expedition 304/305. In: Blackman, D.K., Ildefonse, B., John, B.E., Ohara, Y., Miller, D.J., MacLoed, C.J. and
958 the Expedition 304/305 Scientists. Proc. IODP, 304/305: College Station Tx.
959 Halfpenny, A., Prior D.J., Wheeler, J., 2006. Analysis of dynamic recrystallization and nucleation in a quartzite
960 mylonite. Tectonophysics, 427, 3-14.
961 Halfpenny, A., Prior, D.J., Wheeler, J., 2012. Electron backscatter diffraction analysis to determine the
962 mechanisms that operated during dynamic recrystallisation of quartz-rich rocks. Journal of Structural Geology,
963 36, 2-15.
964 Hannington, M.D., Galley, A.G., Herzig, P.M., Petersen, S., 1998. Comparison of the TAG mound and stockwork
965 complex with Cyprus-type massive sulfide deposits, in: Herzig, P.M., Humphris, S.E., Miller, D.J., Zierenberg,
966 R.A. (Eds.) Proceedings of the Ocean Drilling Program, Scientific Results, Vol. 158, 389-415.
967 Hashiguchi, H., Yamada, R., Inoue, T., 1983. Practical application of low Na_2O anomalies in the footwall acid
968 lava for delimiting promising areas around the Kosaka and Fukazawa Kuroko deposits, Akita Prefecture,
969 Japan. In: Ohmoto, H., Skinner, B.J. (eds.) Kuroko and related volcanogenic massive sulfide deposits.
970 Economic Geology, Monograph 5, 387-394.
971 Humphris, S.E., Alt, J.C., Teagle, D.A.H., Honnorez, J.J., 1998. Geochemical changes during hydrothermal
972 alteration of basement in the stockwork beneath the TAG active hydrothermal mound, in: Humphris, S.E.,
973 Herzig, P.M., Miller, D.J., Zierenberg, R. (Eds.) Proceedings of ODP Scientific Results, 158, College Station,
974 TX (Ocean Drilling Program), 255-276.
975 Hart, T.R., Gibson, H.L., Lesher, C.M., 2004. Trace element geochemistry and petrogenesis of felsic volcanic
976 rocks associated with volcanogenic massive Cu-Zn-Pb sulfide deposits. Economic Geology, 99, 1003-1013.
977 Herrington, R., Maslennikov, V., Zaykov, V., Seravkin, I., Kosarev, A., Buschmann, B, Orgeval, J.-J., Holland, N.,
978 Tessalina, S., Nimis, P., Armstrong, R., 2005. Classification of VMS deposits: lessons from the South Uralides.
979 Ore Geology Reviews, 27, 203-237.

Hollis, S.P., Yeats, C.J., Wyche, S., Barnes, S.J., Ivanic, T.J., Belford, S.M., Davidson, G.J., Roache, A.J., Wingate, M.T.D., 2015. A review of volcanic-hosted massive sulfide (VHMS) mineralization in the Archaean Yilgarn Craton, Western Australia: tectonic, stratigraphic and geochemical associations. Precambrian Research, 260, 113-135.

Humpris, S.E., Herzig, P.M., Miller, D.J., Alt, J.C., Becker, K., Brown, D., Brügmann, G., Chiba, H., Fouquet, Y., Gemmell, J.B., Guertin, G., Hannington, M.D., Holm, N.G., Honnorez, J.J., Itturino, G.J., Knott, R., Ludwig, R., Nakamura, J., Petersen, S., Reysenback, A.-L., Rona, P.A., Smith, S., Sturz, A.A., Tivey, M.K., Zhao, X., 1995. The internal structure of an active sea-floor massive sulphide deposit. Nature, 377, 713-716.

Ishibashi, J.-I., Ikegami, F., Tsuji, T., Urabe, T., 2015. Hydrothermal activity in the Okinawa Trough back-arc basin: geological background and hydrothermal mineralization, in: Ishibashi, J.-i. et al (Eds). Subseafloor Biosphere Linked to Hydrothermal Systems: TAIGA Concept. pp337-359.

Ishibashi, J.-I., Miyoshi, Y., Inoue, H., Yeats, C., Hollis, S.P., Corona, J.C., Bowden, S., Yang, S., Southam, G., Masaki, Y., Hartnett, H., IODP Expedition 331 Scientists, 2013. Subseafloor structure of a submarine hydrothermal system within volcaniclastic sediments: a modern analogue for 'Kuroko-type' VMS deposits. In: Mineral Deposit Research for a high-tech world. 12th SGA Biennial Meeting 2013, Proceedings volume 2, 542-544.

Ishibashi, J.-I., Urabe, T., 1995. Hydrothermal activity related to arc-backarc magmatism in the Western Pacific, in: Taylor, B. (Ed.), Backarc Basins: Tectonics and Magmatism. Plenum Press, New York, pp451-495.

Ishizuka, H., Kawanobe, Y., Sakai, H., 1990. Petrology and geochemistry of volcanic rocks dredged from the Okinawa Trough, an active back-arc basin. Geochemical Journal, 24, 75-92.

Jenner, G.A., 1996. Trace element geochemistry of igneous rocks: geochemical nomenclature and analytical geochemistry, in: Wyman, D.A. (Ed.), Trace element geochemistry of volcanic rocks: applications for massive sulfide exploration. Geological Association of Canada, Short Course Notes, 12, 51-77.

Kawagucci, S., Chiba, H., Ishibashi, J.-i., Yamanaka, T., Toki, T., Muramatsu, Y., Ueno, Y., Makabe, A., Inoue, K., Yoshida, N., Nakagawa, S., Nunoura, T., Takai, K., Takahata, N., Sano, Y., Narita, T., Teranishi, G., Obata, H., Gamo., T., 2011. Hydrothermal fluid geochemistry at the Iheya North field in the mid-Okinawa Trough: implication for origin of methane in subseafloor fluid circulation systems. Geochemical Journal, 45, 109-124.

Kawagucci, S., Miyazaki, J., Nakajima, R., Nozaki T., Takaya, Y., Kato, Y., Shibuya, T., Konno, Y., Nakaguchi, Y., Hatada, K., Hirayama, H., Fujikura, K., Furushima, Y., Yamamoto, H., Watsuji, T., Ishibashi, J-I., Takai, K., 2013. Post-drilling changes in fluid discharge pattern, mineral deposition, and fluid chemistry in the Iheya North hydrothermal field, Okinawa Trough. Geochemistry, Geophysics, Geosystems, 14, 4774-4790.

Kalogeropoulos, S.I., Scott, S.D., 1983. Mineralogy and geochemistry of tuffaceous exhalates (tetusekiei) of the Fukazawa mine, Hokuroko district, Japan. In: Ohmoto, H., Skinner, B.J. (eds.) Kuroko and related volcanogenic massive sulfide deposits. Economic Geology, Monograph 5, 412-432.

Keith, M., Haase, K.M., Schwarz-Schampera, U., Klemd, R., Petersen, S., Back, W., 2014. Effects of temperature, sulphur, and oxygen fugacity on the composition of sphalerite from submarine hydrothermal vents. Geology. First Published online June 30.2014. Doi:10.1130/G35655.1

Klingelhoefer, F., Lee, C.-S., Lin, J.-Y., Sibuet, J.-C., 2009. Structure of the southernmost Okinawa Trough from reflection and wide-angle seismic data. Tectonophysics, 466, 281-288.

1019 Kuroda, H., 1977. Mechanism of formation of the Furutobe Kuroko ore deposit – and exploration at the Furutobe
1020 mine (II). Mining Geology, 27, 9-22 (in Japanese).
1021 Lackschewitz, K.S., Devey, C.W., Stoffers, P., Botz, R., Eisenhauer, A., Kummetz, M., Schmidt, M., Singer, A.,
1022 2004. Mineralogical, geochemical and isotopic characteristics of hydrothermal alteration processes in the
1023 active, submarine, felsic-hosted PACMANUS field, Manus Basin, Papua New Guinea. Geochimica et.
1024 Cosmochimica Acta, 68, 4405-4427.
1025 Large, R.R., Gemmell, J.B., Paulick H., 2011a. The Alteration Box Plot: a simple approach to understanding the
1026 relationship between alteration mineralogy and lithogeochemistry associated with volcanic-hosted massive
1027 sulfide deposits. Economic Geology, 96, 957-971.
1028 Large, R.R., McPhie, J., Gemmell, J.B., Hermann, W., Davidson, G., 2001b. The spectrum of ore deposit types,
1029 volcanic environments, alteration halos, and related exploration vectors in submarine volcanic successions:
1030 some examples from Australia. Economic Geology, 96, 913-938.
1031 Leat, P.T., Jackson, S.E., Thorpe, R.S., Stillman, C.J., 1986. Geochemistry of bimodal basalt-
1032 subalkaline/peralkaline rhyolite provinces within the Southern British Caledonides. Journal of the Geological
1033 Society, London, 143, 259-273.
1034 Lee, C., Shor, G.G., Bibee, L.D., Lu, R.S., Hilde, T.W.C., 1980. Okinawa Trough, origin of a back-arc basin.
1035 Marine Geology, 35, 219–241.
1036 Lentz, D.R., Hall, D.C., Hoy, L.D., 1997. Chemostratigraphic, alteration, and oxygen isotopic trends in a profile
1037 through the stratigraphic sequence hosting the Heath Steel B Zone massive sulfide deposit, New Brunswick.
1038 The Canadian Mineralogist, 35, 841-874.
1039 Lesher, C.M., Goodwin, A.M., Campbell, I.H., Gorton, M.P., 1986. Trace-element geochemistry of ore-associated
1040 and barren, felsic metavolcanic rocks in the Superior Province, Canada. Canadian Journal of Earth Sciences,
1041 23, 222-237.
1042 Letouzey, J., Kimura, M., 1986. The Okinawa Trough: genesis of a back-arc basin developing along a continental
1043 margin. Tectonophysics, 125, 209–230.
1044 Lüders, V., Pracejus, B., Halback, P., 2001. Fluid inclusion and sulfur isotope studies in probable modern analogue
1045 for Kuroko-type ores from the JADE hydrothermal field (Central Okinawa Trough, Japan). Chemical Geology,
1046 173, 45-58.
1047 MacLean, W.H., Barrett, T.J., 1993. Lithogeochemical techniques using immobile elements. Journal of
1048 Geochemical Exploration, 48, 109-133.
1049 MacLean, W.H., Hoy, L.D., 1991. Geochemistry of hydrothermally altered rocks at the Horne Mine, Noranda,
1050 Quebec. Economic Geology, 86, 506-528.
1051 MacLean, W.H., Kranidotis, P. 1987. Immobile elements as monitors of mass transfer in hydrothermal alteration:
1052 Phelps Dodge massive sulfide deposit, Matagami, Quebec. Economic Geology, 82, 951-962.
1053 Masaki, Y., Kinoshita, M., Inagaki, F., Nakagawa, S., Takai, K., 2011. Possible kilometer-scale hydrothermal
1054 circulation within the Iheya-North field, mid-Okinawa Trough, as inferred from heat flow data. JAMSTEC
1055 Rep. Res. Dev. 12, 1-12Mayer J.W. (1977) Ion Beam Handbook for Material Analysis. Academic Press, New
1056 York

McConachy, T.F., Arculus, R.J., Yeats, C.J., Barriga, F.J.A.S., McInnes, B.I.A., Sestak, S., Sharpe, R., Rakau, B., Tevi, T., 2005. New hydrothermal activity and alkalic volcanism in the backarc Coriolis Troughs, Vanuatu. Geology, 33, 61-64.

McConnell, B.J., Stillman, C.J., Hertogen, J. 1991. An Ordovician basalt to peralkaline rhyolite fractionation series from Avoca, Ireland. Journal of the Geological Society, London, 148, 711-718.

McLeod, R.L., Stanton, R.L., 1984. Phyllosilicates and associated minerals in some Paleozoic stratiform sulfide deposits of Southeastern Australia. Economic Geology, 79, 1-22.

Mottl, M.J., Wheat, C.G., Boulègue, J., 1994. Timing of ore deposition and sill intrusion at Site 856: evidence from stratigraphy, alteration, and sediment pore-water composition, in Mottl, M.J., Davis, E.E., Fisher, A.T. & Slack, J.F. (Eds.), Proc. ODP, Sci. Results, 139: College Station, TX (Ocean Drilling Program), 679–693. doi:10.2973/odp.proc.sr.139.232.1994

Nakagawa, S., Takai, K., Inagaki, F., Chiba, H., Ishibashi, J., Kataoka, S., Hirayama, H., Nunoura, T., Horikoshi, K., Sako, Y., 2005. Variability in microbial community and venting chemistry in a sediment-hosted backarc hydrothermal system: impacts of subseafloor phase-separation. FEMS Microbiol. Ecol. 54, 141-155.

Oiwane, H., Kumagai, H., Masaki, Y., Tokuyama, H., Kinoshita, M., 2008. Characteristics of sediment in Iheya North Knoll and the 'acoustic blanking layer'. Japanese Geoscience Union Meeting. J164-013.

Paulick, H., Bach, W., 2006. Phyllosilicate alteration mineral assemblages in the active subsea-floor Pacmanus hydrothermal system, Papua New Guinea, ODP Leg 193. Economic Geology, 101, 633-650.

Paulick, H., Herrmann, W., Gemmell, J.B., 2001. Alteration of felsic volcanics hosting the Thalanga massive sulfide deposit (Northern Queensland, Australia) and geochemical proximity indicators to ore. Economic Geology, 96, 1175-1200.

Pearce, J.A., 1996. A user's guide to basalt discrimination diagrams, in: Wyman, D.A. (Ed.), Trace element geochemistry of volcanic rocks: applications for massive sulphide exploration. Geological Association of Canada, pp. 79-113.

Pearce, J.A., Harris, N.B.W., Tindle, A.G., 1984. Trace element discrimination diagrams for the tectonic interpretation of granitic rocks. Journal of Petrology, 25, 956-983.

Petersen, S., Monecke, T., Westhues, A., Hannington, M.D., Gemmell, J.B., Sharpe, R., Peters, M., Strauss, H., Lackschewitz, K., Augustin, N., Gibson, H., Kleeberg, R., 2014. Drilling shallow-water massive sulfides at the Palinuro Volcanic Complex, Aeolian Island Arc, Italy. Economic Geology, 109, 2129-2157.

Piercey, S.J., 2007. Volcanogenic massive sulphide (VMS) deposits of the Newfoundland Appalachians: an overview of their setting, classification, grade-tonnage data, and unresolved questions, in: Pereira, C.G.P., Walsh, D.G. (Eds.), Current Research. Newfoundland Department of Natural Resources, Geological Survey, Report 07-01, 169-178.

Piercey, S.J., 2009. Lithogeochemistry of volcanic rocks associated with volcanogenic massive sulphide deposits and applications to exploration. In: Cousens, B., Piercey, S.J. (eds). Submarine volcanism and mineralization: modern through ancient. Geological Association of Canada, Short Course 29-30 May 2008, Canada, p15-40.

Piercey, S.J., 2011. The setting, style, and role of magmatism in the formation of volcanogenic massive sulphide deposits. Mineralium Deposita, 46, 449-471.

1095 Prior, D.J., Mariani, E., Wheeler, J., 2009. EBSD in the earth sciences: applications, common practice and
1096 challenges, in: Schwartz, A.J., Kumar, M., Adams, B. L., Field, D.P. (Eds.), Electron Backscatter Diffraction
1097 in Materials Science. Springer Berlin, pp. 345-360.
1098 Prior, D.J., Boyle, A.P., Brenker, F., Cheadle, M.C., Day, A., Lopez, G., Peruzzo, L., Potts, G.J., Reddy, S., Spiess,
1099 R., Timms, N.E., Trimby, P., Wheeler, J., Zetterstrom, L., 1999. The application of electron backscatter
1100 diffraction and orientation contrast imaging in the SEM to textural problems in rocks. American Mineralogist,
1101 84, 1741-1759.
1102 Roberts, S., Bach, W., Binns, R.A., Vanko, D.A., Yeats, C.J., Teagle, D.A.H., Blacklock, K., Blusztajn, J.S.,
1103 Boyce, A.J., Cooper, M.J., Holland, N., McDonald, B., 2003. Contrasting evolution of hydrothermal fluids in
1104 the PACMANUS system, Manus Basin: the Sr and S isotope evidence. Geology, 31, 805-808.
1105 Sánchez-España, J., Velasco, F., Yusta, I., 2000. Hydrothermal alteration of felsic volcanic rocks associated with
1106 massive sulphide deposition in the northern Iberian Pyrite Belt (SW Spain). Applied Geochemistry, 15, 1265-
1107 1290.
1108 Sato, T., 1974. Distribution and geological setting of the Kuroko deposits. In: Ishihara, S (ed.) Geology of Kuroko
1109 deposits. Mining Geology Special Issue 6, 1-10.
1110 Sato, T., 1977. Kuroko deposits: their geology, geochemistry and origin. Geological Society, London, Special
1111 Publications, 7, 153-161.
1112 Schmidt, J.M., 1988. Mineral and whole-rock compositions of seawater-dominated hydrothermal alteration at the
1113 Arctic volcanogenic massive sulfide prospect, Alaska. Economic Geology, 83, 822-842.
1114 Shanks III, W.C., 2012. Hydrothermal alteration in volcanogenic massive sulfide occurrence model. U.S.
1115 Geological Survey Scientific Investigations Report 2010-5070, Chapter 11, 12p.
1116 Shao, H., Yang, S., Wang, Q., Guo, Y., 2015. Discriminating hydrothermal and terrigenous clays in the Okinawa
1117 Trough, East China Sea: evidences from mineralogy and geochemistry. Chemical Geology.
1118 Doi:10.1016/j.chemgeo.2015.02.001
1119 Shikazono, N., Holland, H.D., Quirk, R.D., 1983. Anhydrite in Kuroko deposits: mode of occurrence and
1120 depositional mechanisms. In: Ohmoto, H., Skinner, B.J. (eds.) Kuroko and related volcanogenic massive
1121 sulfide deposits. Economic Geology, Monograph 5, 329-344.
1122 Shinjo, R., Chung, S.-l., Kato, Y., Kimura, M., 1999. Geochemical and Sr-Nd isotopic characteristics of volcanic
1123 rocks from the Okinawa Trough and Ryukyu Arc: implications for the evolution of a young, intracontinental
1124 back arc basin. Journal of Geophysical Research, 104, 10591-10608.
1125 Shinjo, R., Kato, Y., 2000. Geochemical constraints on the origin of bimodal magmatism at the Okinawa Trough,
1126 an incipient back-arc basin. Lithos, 54, 117-137.
1127 Shinjo, R., Woodhead, J.D., Hergt, J.M., 2000. Geochemical variation within the northern Ryukyu Arc: magma
1128 source compositions and geodynamic implications. Contributions to Mineralogy and Petrology, 140, 263-282.
1129 Sibuet, J.-C., Deffontaines, B., Hsu, S.-K., Thareau, N., Le Formal, J.-P., Liu, C.-S., ACT party., 1998. Okinawa
1130 Trough backarc basin: early tectonic and magmatic evolution. Journal of Geophysical Research, 103, 30245-
1131 30267.
1132 Sibuet, J.-C., Letouzey, J., Barbier, F., Charvet, J., Foucher, J.P., Hilde, T.W.C., Kimura, M., Chiao, L.Y., Marsset,
1133 B., Muller, C., Stephan, J.F., 1987. Back arc extension in the Okinawa Trough. Journal of Geophysical
1134 Research, 92, 14041-14063.

1135 Sturz, A. Itoh, M., Smith, S., 1998. Mineralogy and geochemical composition of clay minerals, TAG hydrothermal
1136 mound, in: Herzig, P.M., Humphris, S.E., Miller, D.J. & Zierenberg, R.A. (Eds.). Proceedings of the Ocean
1137 Drilling Program, Scientific Results, 158, 277-284.
1138 McDonough, W.F., Sun, S-S., 1995. The composition of the Earth. Chemical Geology, 120, 223–254.
1139 Takai, K., Mottl, M.J., Nielsen, S.H.H., the Expedition 331 Scientists, 2011. Proceedings of IODP 331. Tokyo
1140 (Integrated Ocean Drilling Program Management International, Inc). Doi:10.2204/iodp.proc.331.2011.
1141 Takai, K., Mottl, M.J., Nielsen, S.H.H., the Expedition 331 Scientists, 2012. IODP Expedition 331: strong and
1142 expansive subseafloor hydrothermal activities in the Okinawa Trough. Scientific Drilling, 13, 19-27. DOI:
1143 10.2204/iodp.sd.13.03.2011.
1144 Teagle, D.A.H., Alt, J.C., Chiba, H., Humphris, S.E., Haliday, A.N., 1998. Strontium and oxygen isotopic
1145 constraints on fluid mixing, alteration and mineralization in the TAG hydrothermal deposit. Chemical
1146 Geology, 149, 1-24.
1147 Tindle, A. 2015. Chlorite mineral calculation worksheet. Available at: http://www.open.ac.uk/earth-
1148 research/tindle/AGTWebPages/AGTSoft.html
1149 Trimby, P.W., Prior, D.J., Wheeler, J., 1998. Grain boundary hierarchy development in a quartz mylonite. Journal
1150 of Structural Geology, 20, 917-935.
1151 Tsuji, T., Takai, K., Oiwane, H., Nakamura, Y., Masaki, Y., Kumagai, H., Kinoshita, M., Yamamoto, F., Okana, T.,
1152 Kuramoto, S., 2012. Hydrothermal fluid flow system around the Iheya North Knoll in the mid-Okinawa trough
1153 based on seismic reflection data. Journal of Volcanology and Geothermal Research, 213-214, 41-50.
1154 Ueno, H., Hamasaki, H., Murakawa, Y., Kitazono, S., Takeda, T., 2003. Ore and gangue minerals of sulfide
1155 chimneys from the North Knoll Iheya Ridge, Okinawa Trough, Japan. JAMSTEC Journal of Deep Sea
1156 Research, 22, 49-62.
1157 van Staal, C.R., 2007. Pre-Carboniferous tectonic evolution and metallogeny of the Canadian Appalachians, in:
1158 Goodfellow, W.D. (Ed.), Mineral Deposits of Canada: a synthesis of major deposit types, district metallogeny,
1159 the evolution of geological provinces, and exploration methods. Geological Association of Canada, Mineral
1160 Deposits Division, Special Publication No. 5, pp793-818.
1161 Webber, A.P., Roberts, S., Burgess, R., Boyce, A.J., 2011. Fluid mixing and thermal regimes beneath the
1162 PACMANUS hydrothermal field, Papua New Guinea: helium and oxygen isotope data. Earth and Planetary
1163 Science Letters, 304, 93-102.
1164 Webber, A.P., Roberts, S., Murton, B.J., Hodgkinson, M.R.S., 2015. Geology, sulphide geochemistry and
1165 supercritical venting at the Bebe hydrothermal vent field, Cayman Trough. Geochemistry, Geophysics,
1166 Geosystems. Online First. DOI: 10.1002/2015GC005879.
1167 Yamada, R., Yoshida, T., 2011. Relationships between Kuroko volcanogenic massive sulfide (VMS) deposits,
1168 felsic volcanism, and island arc development in the northeast Honshu arc, Japan. Mineralium Deposita, 46,
1169 431-448.
1170 Yamano, M., Uyeda, S., Kinoshita, H., Hilde, T.W.C., 1986. Report on DEL1984 cruises in the middle Okinawa
1171 Trough. 4. Heat flow measurements. Bull. Earthquake Res. Int. Univ. Tokyo, 61, 251-267.
1172 Yeats, C., 2012. Deep sea mining: exploration is inevitable. http://www.scidev.net/global/earth-
1173 science/opinion/deep-sea-mining-exploration-is-inevitable.html

Yeats, C.J., Parr, J.M., Binns, R.A., Gemmell, J.B., Scott, S.D., 2014. The Susu Knolls hydrothermal field, Eastern Manus Basin, Papua New Guinea: an active submarine high-sulfidation copper-gold system. Economic Geology, 109, 2207-2226.

Zhang, W., Fyfe, W.S., 1995. Chloritization of the hydrothermally altered bedrock at the Igarapé Bahia gold deposit, Carajás, Brazil. Mineralium Deposita, 30, 30-38.

Zeng, Z.G., Jiang, F.Q., Zhai, S.K., Qin, Y.S., 2000. Lead isotopic compositions of massive sulfides from the Jade hydrothermal field in the Okinawa Trough and its geological significance. Geochimica, 29, 239-245 (in Chinese with English Abstract).

Zeng, Z., Yu, S., Wang, X., Fu, Y., Yin, X., Zhang, G., Wang, X., Chen, S., 2010. Geochemical and isotopic characteristics of volcanic rocks from the northern East China Sea shelf margin and the Okinawa Trough. Acta Oceanologica Sinica, 29, 48-61.

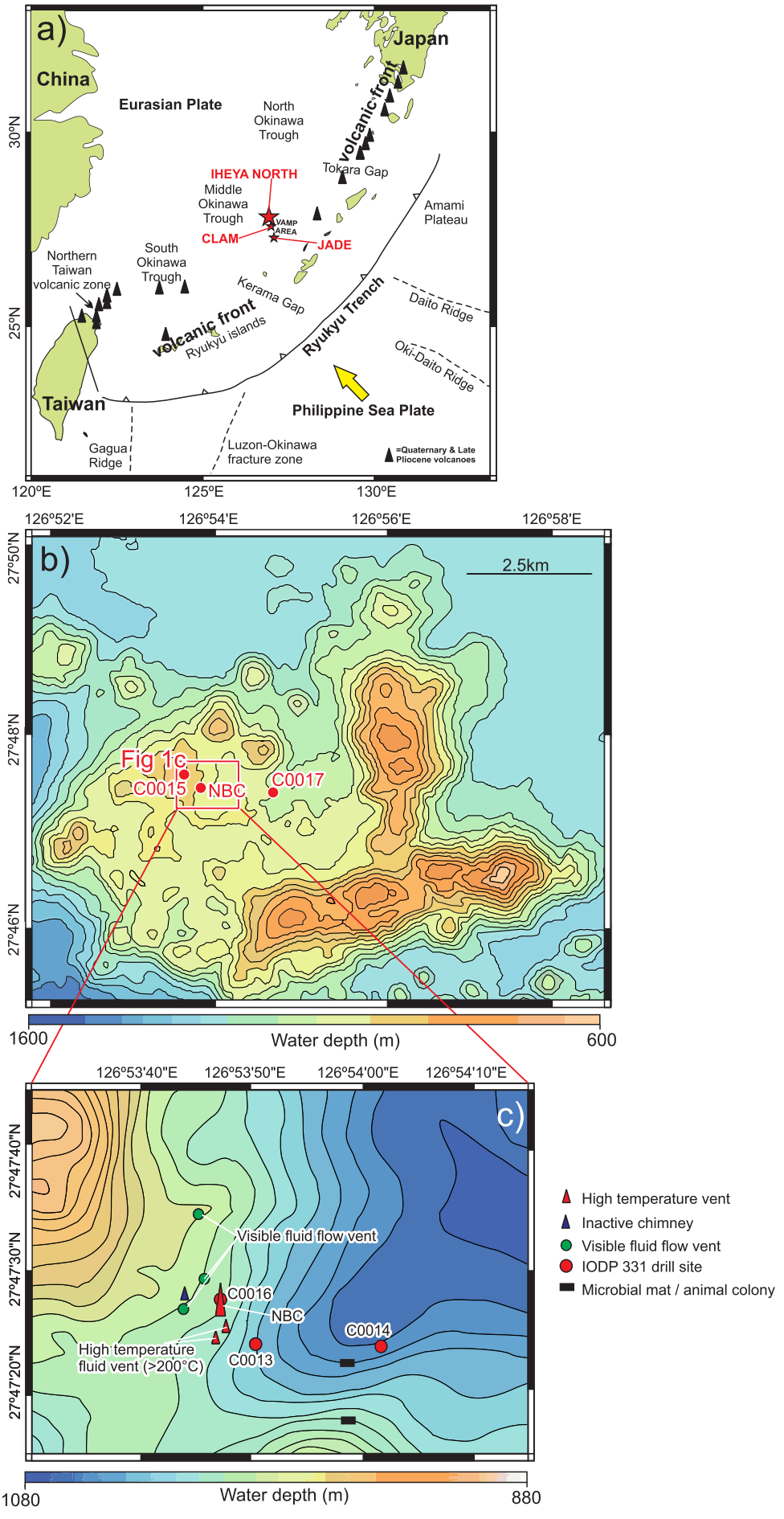
a)
China
Japan
Eurasian Plate
North Okinawa Trough
volcanic front
Tokara Gap
IHEYA NORTH
Middle Okinawa Trough
VAMP AREA
CLAM
JADE
Amami Plateau
Northern Taiwan volcanic zone
South Okinawa Trough
Kerama Gap
volcanic front
Ryukyu islands
Ryukyu Trench
Daito Ridge
Oki-Daito Ridge
Taiwan
Philippine Sea Plate
Gagua Ridge
Luzon-Okinawa fracture zone
=Quaternary & Late Pliocene volcanoes
30°N
25°N
120°E
125°E
130°E
b)
2.5km
Fig 1c
C0015
NBC
C0017
126°52'E
126°54'E
126°56'E
126°58'E
27°50'N
27°48'N
27°46'N
1600
Water depth (m)
600
c)
126°53'40"E
126°53'50"E
126°54'00"E
126°54'10"E
27°47'40"N
27°47'30"N
27°47'20"N
Visible fluid flow vent
C0016
NBC
C0014
High temperature fluid vent (>200°C)
C0013
1080
Water depth (m)
880
High temperature vent
Inactive chimney
Visible fluid flow vent
IODP 331 drill site
Microbial mat / animal colony

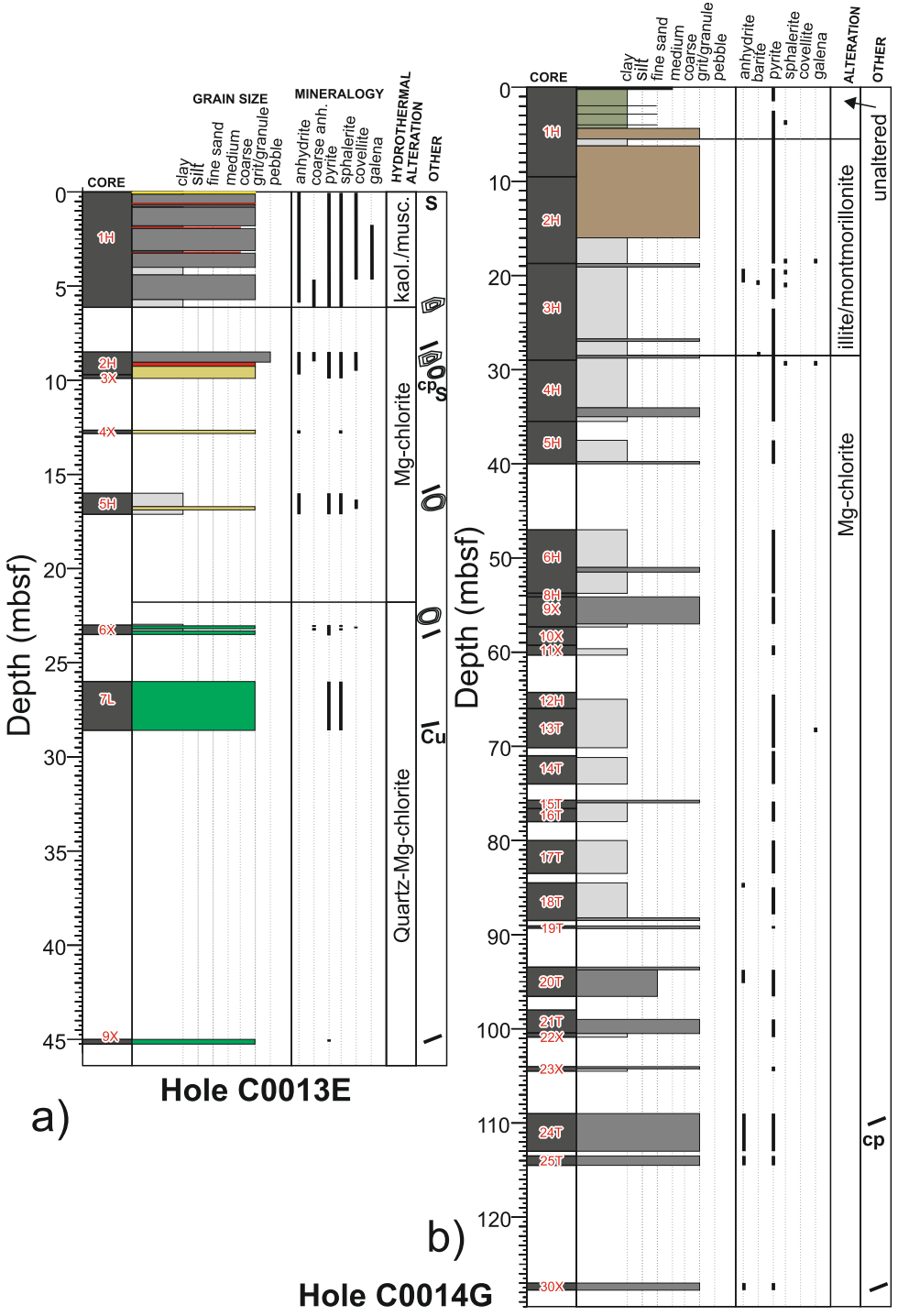

Legend

Medium- to coarse-grained sulfidic sediment. Sulfides dominated by pyrite-sphalerite with minor galena and covellite. Some coarse (1-4 cm) fragments of cemented sulfide aggregates.

Reduced mud (unaltered). Dark olive green colour, with foraminifera and very fine disseminated pyrite.

Hydrothermal clay. Light to medium grey colour. May contain pseudoclasts of harder clay after pumice(?).

Unaltered/weakly-altered pumiceous grit/gravel. Pumice clasts in a coarse sand matrix with dark olive green mud. Often clast supported.

Hydrothermal grit/gravel. Scattered large (1-2cm) aggregate clasts set in a clay-sand matrix. Locally sulfide rich (to ~5%). Grey to black colour, occasionally paler. Can be clast- or matrix-supported. Pumice replaced by white to pale grey clay.

Hydrothermal grit with native sulfur. Pale grey to yellow colour. Patches of white clay. Small aggregates of altered volcanic rocks.

Anhydrite-carbonate-silica vein material embedded in dark and white clay.

White to pale grey volcanic breccia.
Strongly altered volcanic rock comprising clasts in a silicified network of quartz veins (hairline to 1cm in width).
Clasts are <0.5cm to >5cm, poorly-sorted, subangular to subrounded, and in some areas jig-saw fit.

Sulfide vein.

Broken anhydrite crystals (to 5mm in size) - veins disturbed by drilling?

S Native sulfur stringers and/or blebs.

Large (4-5cm), white, hard, anhydrite-clay-sulfide nodules (grown *in situ*?). May also contain dolomite, calcite, quartz and/or talc.

cp Presence of trace chalcopyrite.

Cu Presence of native copper in basement.

Note: Sections of re-drilled core not shown.

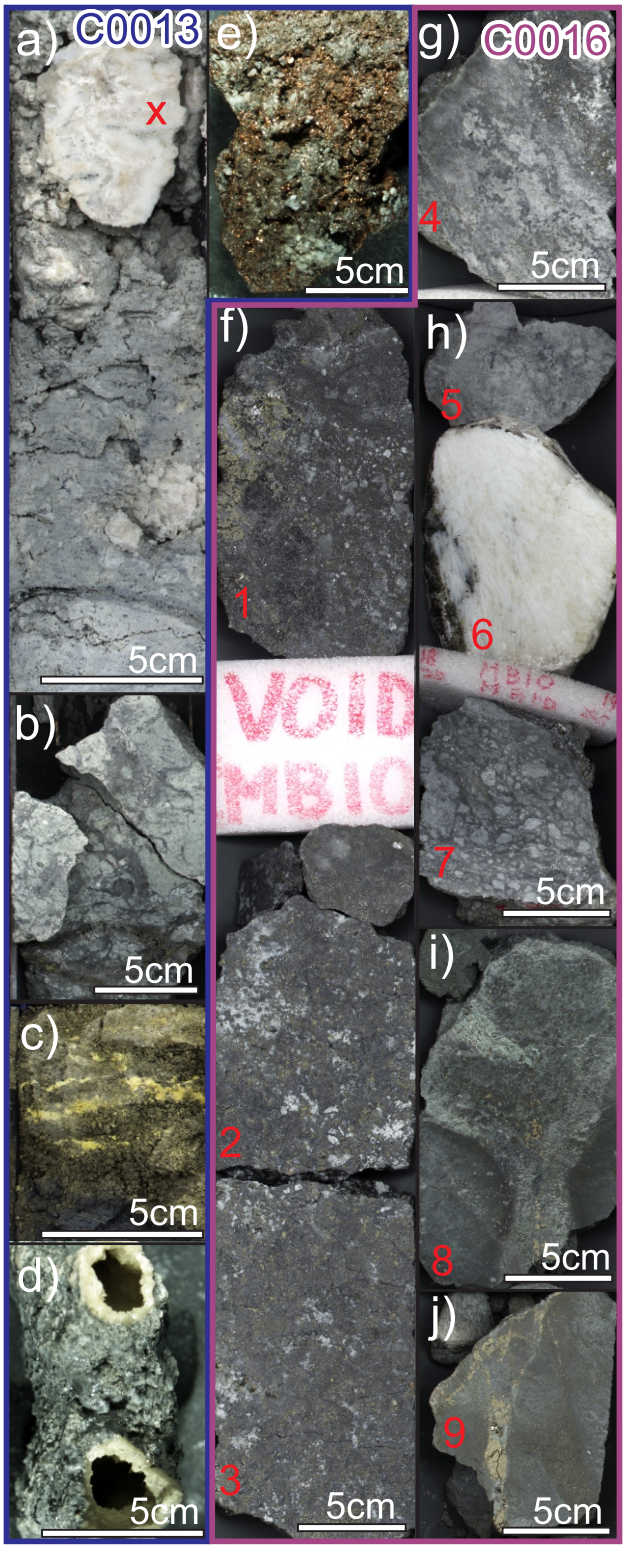
a)
C0013
x
5cm
b)
5cm
c)
5cm
d)
5cm
e)
5cm
f)
1
VOID
MBIO
2
3
5cm
g)
C0016
4
5cm
h)
5
6
7
5cm
i)
8
5cm
j)
9
5cm

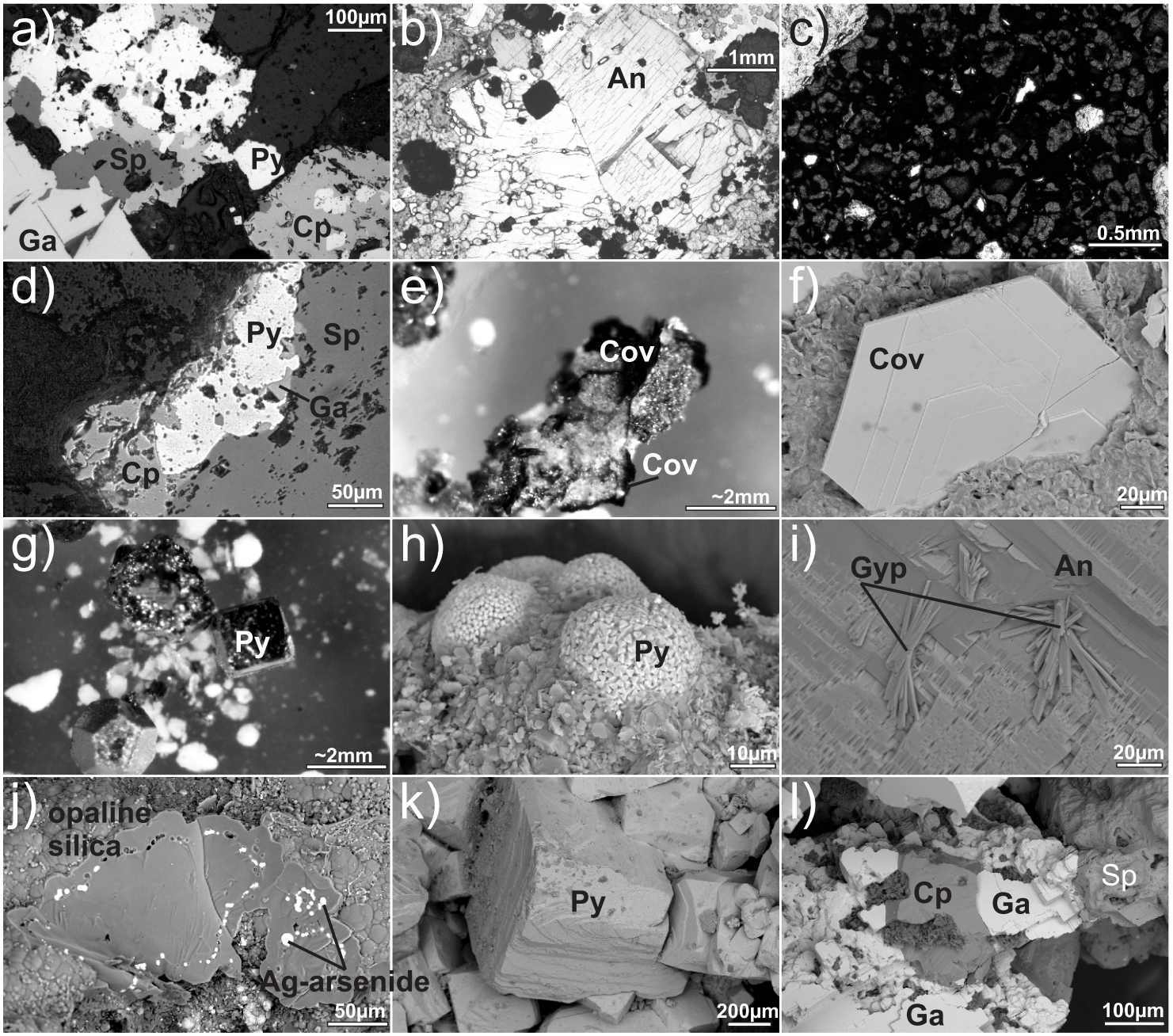
a)
100µm
Sp
Py
Ga
Cp
b)
An
1mm
c)
0.5mm
d)
Py
Sp
Ga
Cp
50µm
e)
Cov
Cov
~2mm
f)
Cov
20µm
g)
Py
~2mm
h)
Py
10µm
i)
Gyp
An
20µm
j)
opaline
silica
Ag-arsenide
50µm
k)
Py
200µm
l)
Cp
Ga
Sp
Ga
100µm

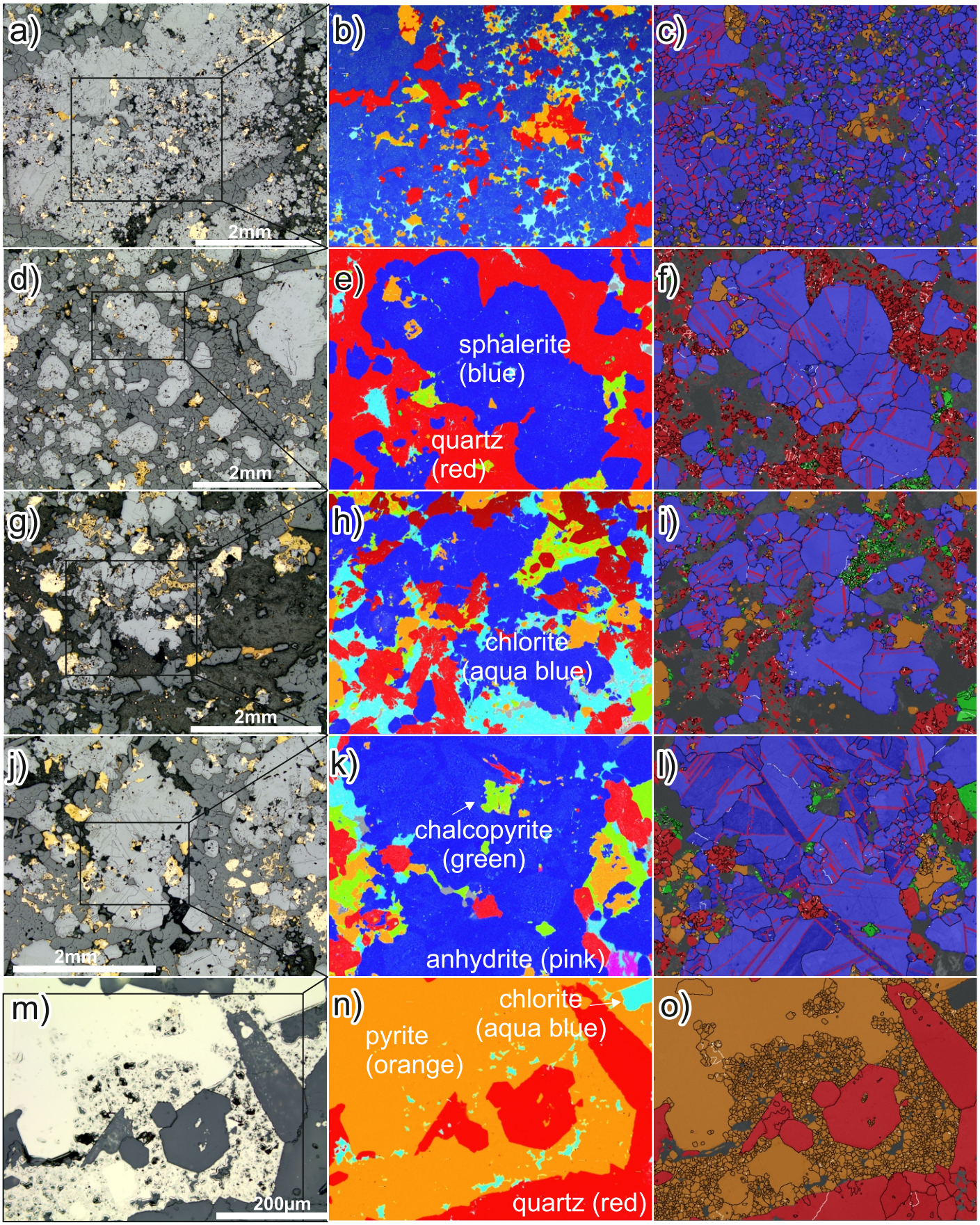
a)
2mm
b)
c)
d)
2mm
e)
sphalerite
(blue)
quartz
(red)
f)
g)
2mm
h)
chlorite
(aqua blue)
i)
j)
2mm
k)
chalcopyrite
(green)
anhydrite (pink)
l)
m)
200µm
n)
pyrite
(orange)
chlorite
(aqua blue)
quartz (red)
o)

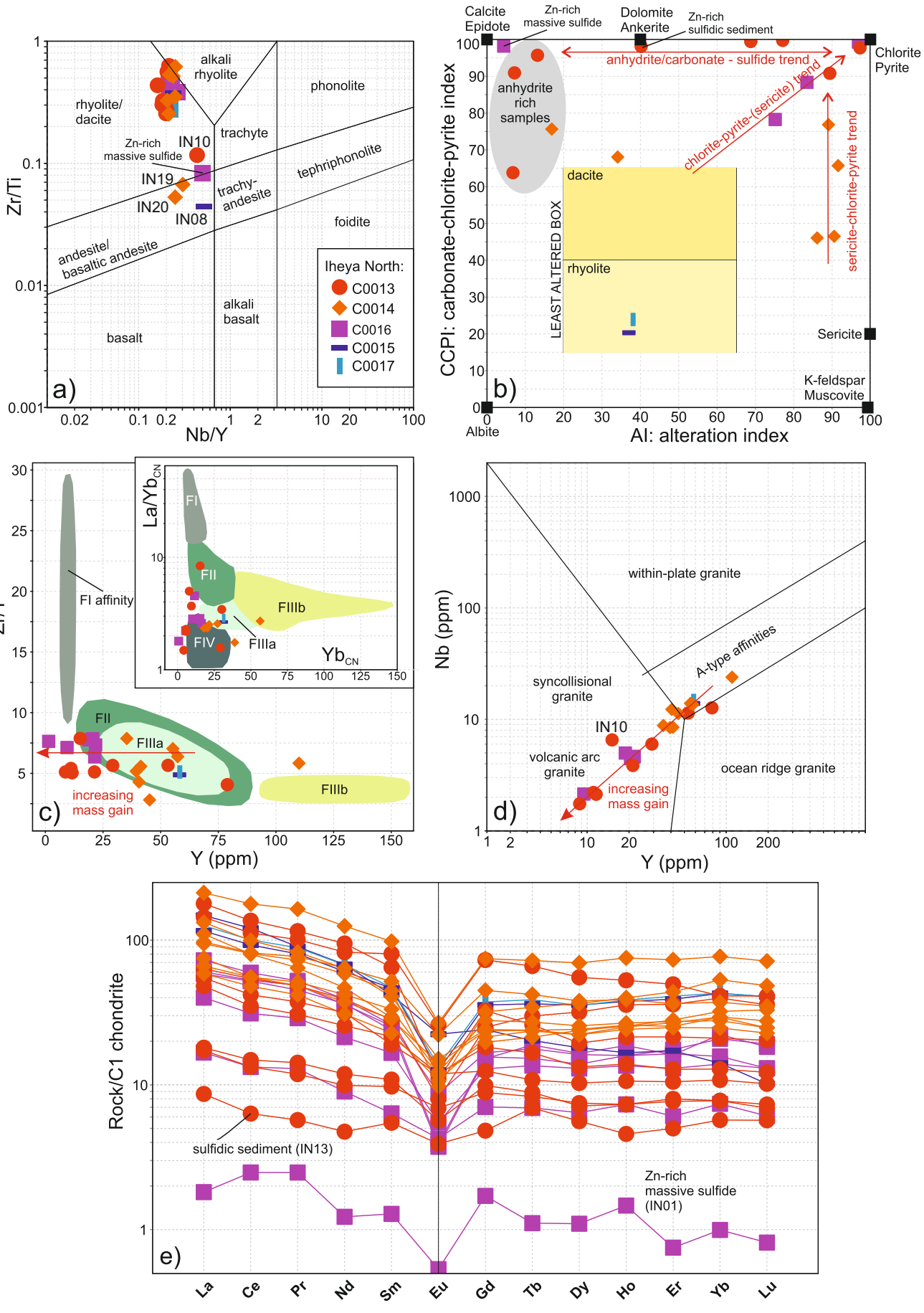
a)
Zr/Ti
Nb/Y
alkali rhyolite
phonolite
rhyolite/ dacite
trachyte
Zn-rich massive sulfide
IN10
IN19
IN20
IN08
trachy- andesite
tephriphonolite
foidite
andesite/ basaltic andesite
alkali basalt
basalt
Iheya North:
C0013
C0014
C0016
C0015
C0017
b)
CCPI: carbonate-chlorite-pyrite index
AI: alteration index
Calcite Epidote
Zn-rich massive sulfide
Dolomite Ankerite
Zn-rich sulfidic sediment
Chlorite Pyrite
anhydrite/carbonate - sulfide trend
anhydrite rich samples
chlorite-pyrite-(sericite) trend
sericite-chlorite-pyrite trend
dacite
rhyolite
LEAST ALTERED BOX
Sericite
K-feldspar Muscovite
Albite
c)
Zr/Y
Y (ppm)
La/Yb$_{CN}$
Yb$_{CN}$
FI
FII
FIIIa
FIIIb
FIV
FI affinity
increasing mass gain
d)
Nb (ppm)
Y (ppm)
within-plate granite
A-type affinities
syncollisional granite
IN10
volcanic arc granite
ocean ridge granite
increasing mass gain
e)
Rock/C1 chondrite
sulfidic sediment (IN13)
Zn-rich massive sulfide (IN01)
La
Ce
Pr
Nd
Sm
Eu
Gd
Tb
Dy
Ho
Er
Yb
Lu

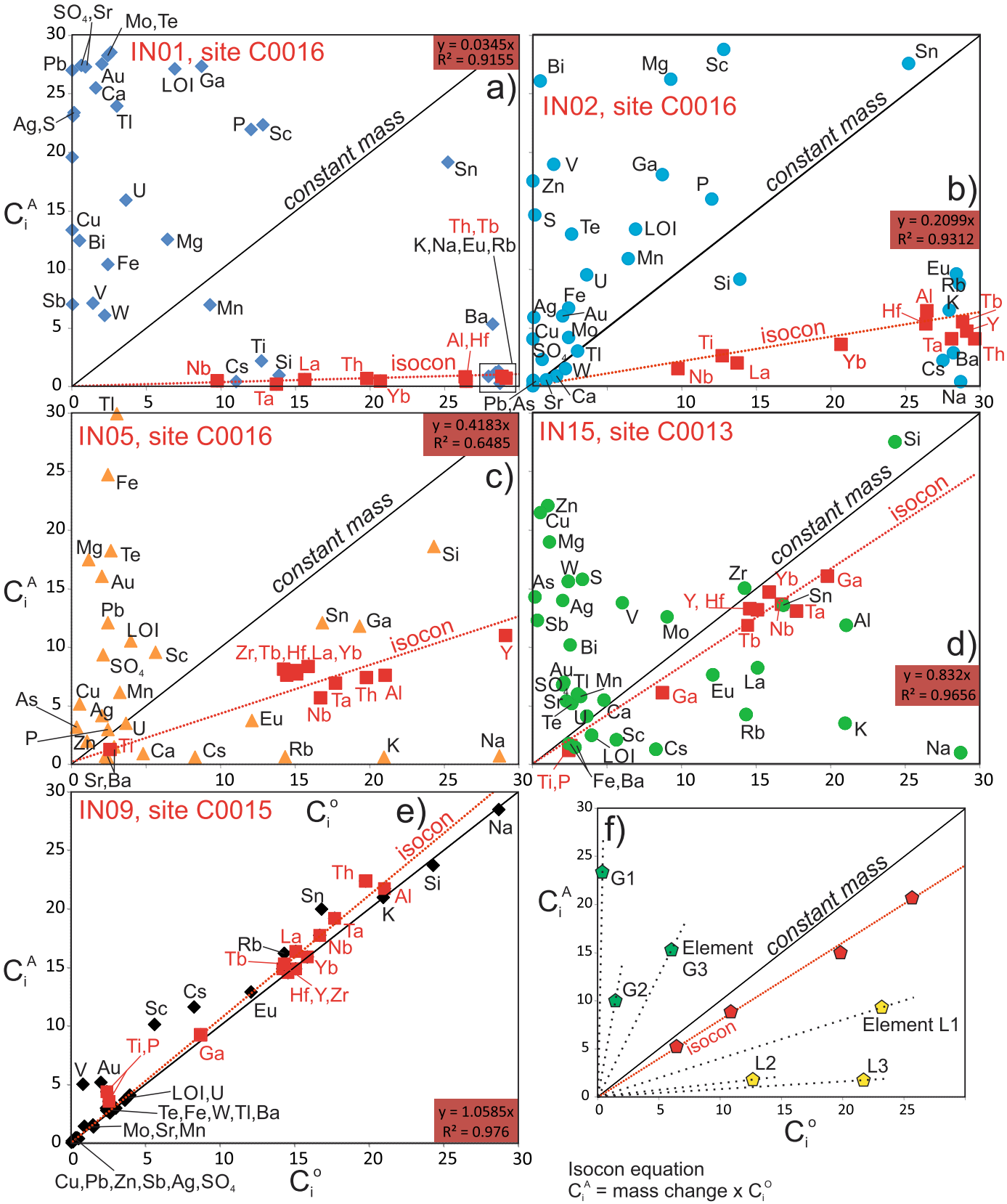

Immobile element used for isocon

Mobile element - removed from rock (below isocon)

Mobile element - added to rock (above isocon)

Isocon equation

C_i^A = mass change x C_i^o

Relative magnitude of mass gains/losses for mobile elements:
G1>G2>G3 (i.e. steeper slope from origin of graph)
L3>L2>L1 (i.e. shallower slope from origin of graph)

Note: The isocon plots below the line of constant mass, therefore the rock has gained mass.

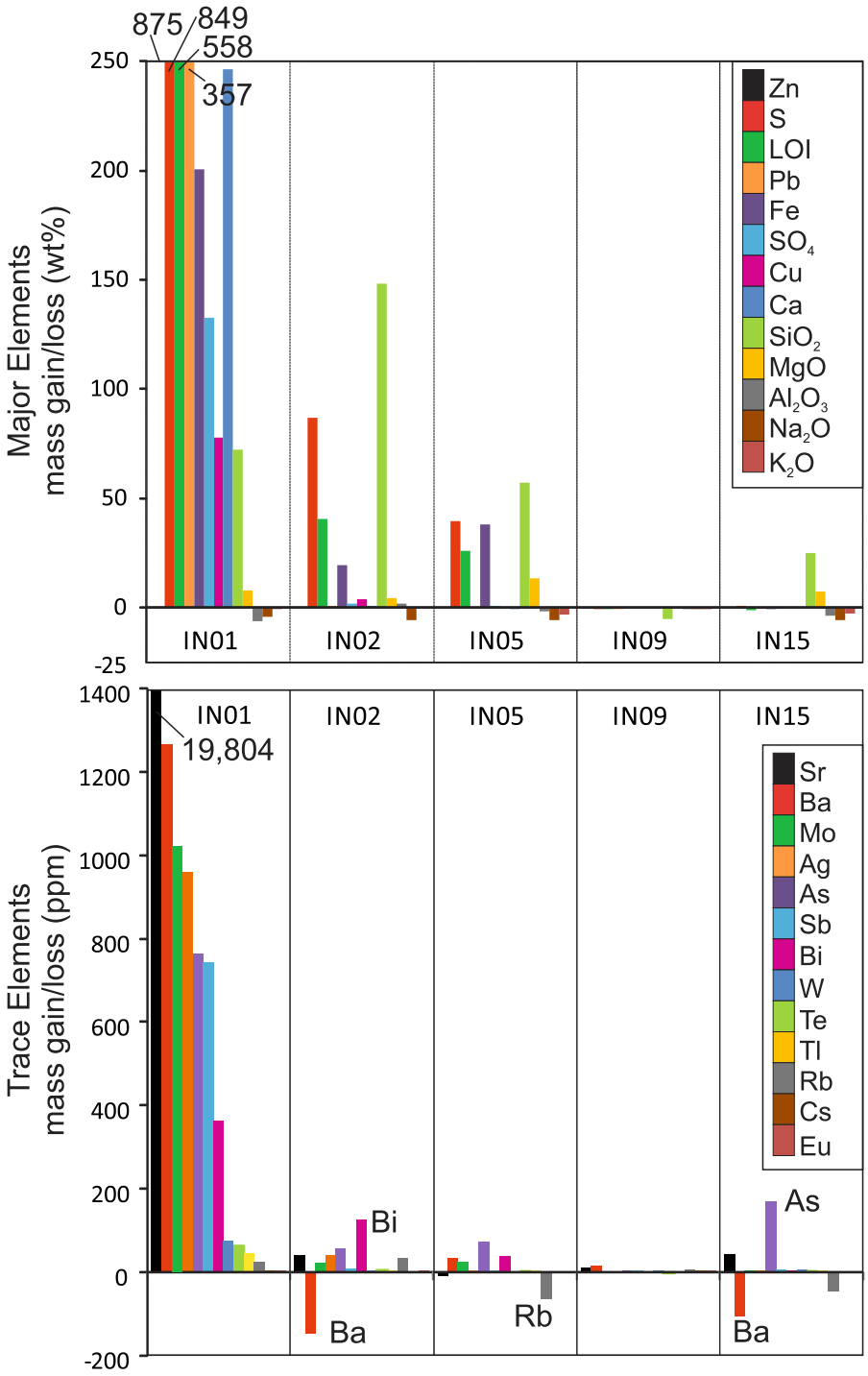
875
849
558
357
250
200
150
100
50
0
-25
Major Elements
mass gain/loss (wt%)
Zn
S
LOI
Pb
Fe
SO4
Cu
Ca
SiO2
MgO
Al2O3
Na2O
K2O
IN01
IN02
IN05
IN09
IN15
1400
1200
1000
800
600
400
200
0
-200
Trace Elements
mass gain/loss (ppm)
IN01
19,804
IN02
IN05
IN09
IN15
Sr
Ba
Mo
Ag
As
Sb
Bi
W
Te
Tl
Rb
Cs
Eu
Bi
Ba
Rb
As
Ba

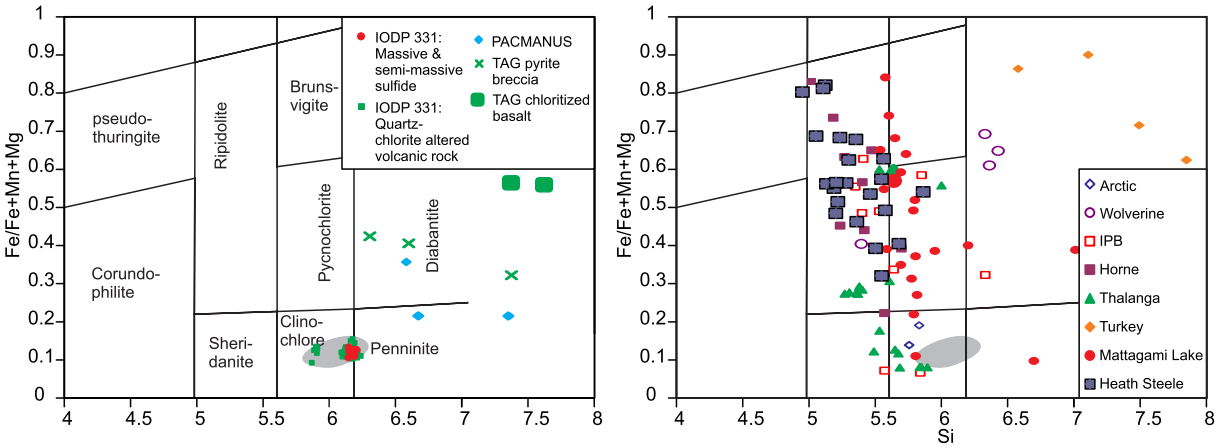
Fe/Fe+Mn+Mg
Si
pseudo-
thuringite
Ripidolite
Bruns-
vigite
Corundo-
philite
Pycnochlorite
Diabantite
Sheri-
danite
Clino-
chlore
Penninite
IODP 331:
Massive &
semi-massive
sulfide
IODP 331:
Quartz-
chlorite altered
volcanic rock
PACMANUS
TAG pyrite
breccia
TAG chloritized
basalt
Arctic
Wolverine
IPB
Horne
Thalanga
Turkey
Mattagami Lake
Heath Steele

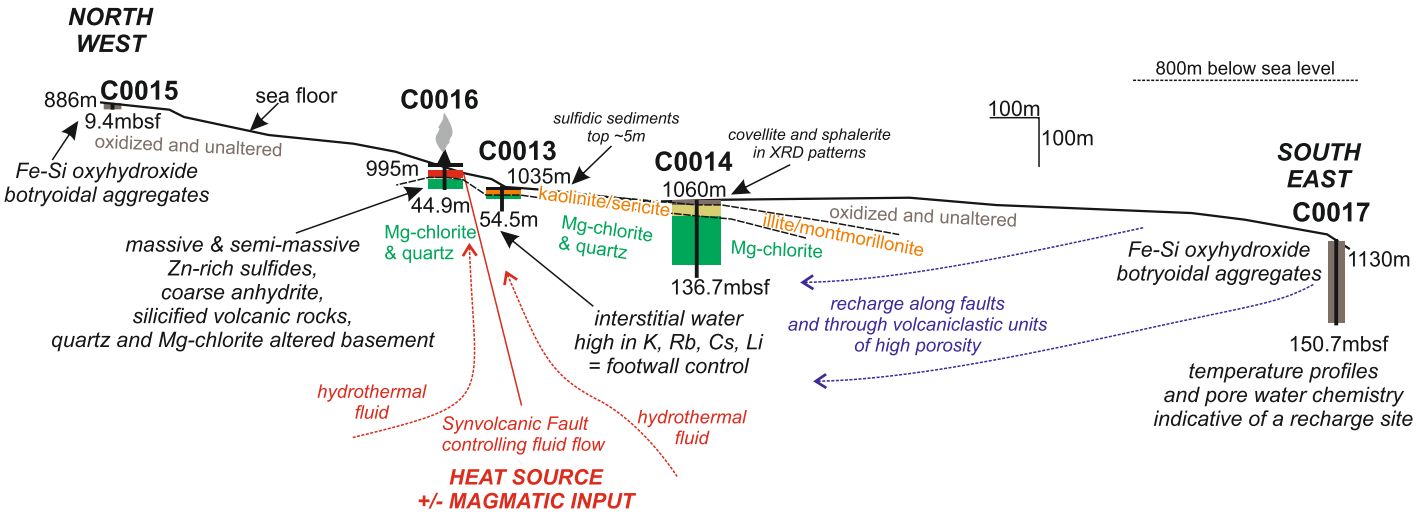
NORTH WEST
C0015
886m
9.4mbsf
oxidized and unaltered
Fe-Si oxyhydroxide botryoidal aggregates
sea floor
C0016
995m
44.9m
massive & semi-massive Zn-rich sulfides, coarse anhydrite, silicified volcanic rocks, quartz and Mg-chlorite altered basement
Mg-chlorite & quartz
C0013
1035m
54.5m
sulfidic sediments top ~5m
kaolinite/sericite
Mg-chlorite & quartz
C0014
1060m
136.7mbsf
covellite and sphalerite in XRD patterns
Mg-chlorite
illite/montmorillonite
oxidized and unaltered
800m below sea level
100m
100m
SOUTH EAST
C0017
1130m
150.7mbsf
Fe-Si oxyhydroxide botryoidal aggregates
temperature profiles and pore water chemistry indicative of a recharge site
recharge along faults and through volcaniclastic units of high porosity
interstitial water high in K, Rb, Cs, Li = footwall control
hydrothermal fluid
Synvolcanic Fault controlling fluid flow
hydrothermal fluid
HEAT SOURCE +/- MAGMATIC INPUT

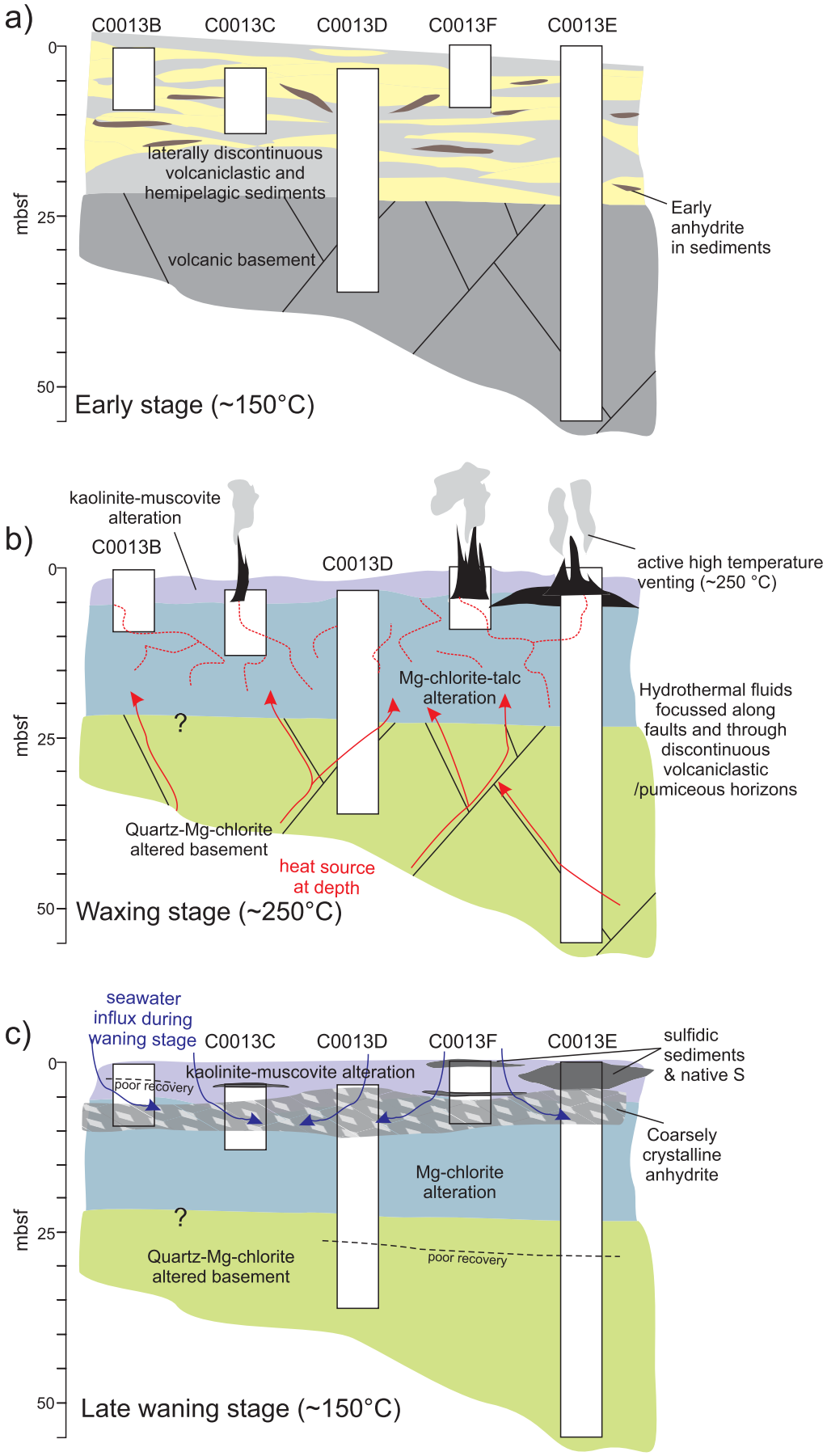
a)
C0013B
C0013C
C0013D
C0013F
C0013E
0
25
50
mbsf
laterally discontinuous volcaniclastic and hemipelagic sediments
volcanic basement
Early anhydrite in sediments
Early stage (~150°C)
b)
kaolinite-muscovite alteration
C0013B
C0013D
active high temperature venting (~250 °C)
Mg-chlorite-talc alteration
Hydrothermal fluids focussed along faults and through discontinuous volcaniclastic /pumiceous horizons
?
Quartz-Mg-chlorite altered basement
heat source at depth
Waxing stage (~250°C)
c)
seawater influx during waning stage
C0013C
C0013D
C0013F
C0013E
sulfidic sediments & native S
kaolinite-muscovite alteration
poor recovery
Coarsely crystalline anhydrite
Mg-chlorite alteration
?
Quartz-Mg-chlorite altered basement
poor recovery
Late waning stage (~150°C)